Department of Advanced Materials Science
Graduate School of Frontier Sciences
The University of Tokyo

2007

Master's thesis

Transport Properties of Photocarrier-Doped $SrTiO_3$

(光キャリアドープされたチタン酸ストロンチウムの輸送特性)

Submitted on January 30, 2007

Supervisor
Associate Professor Harold Y. Hwang

56117 Yusuke Kozuka

Contents

Chapter 1

Introduction

1.1 Materials science and its relation with physics

Materials science has given a lot of unexpected inventions, completely changing our lifestyle on many occasion. It extends from kitchen utensils to state-of-the-art computers. Enormous effort has been spent to create more functional materials fitting our purposes and also to enhance the range of available materials as is the case for metallic glasses and conducting polymers [1] in recent years. Electronic devices, for example, have been growing for more than half a century largely because of the integrability of semiconductors [2]. Although materials science is based on quantum theory, because solid state materials consist of 10^{23} orders of interacting atoms, it is impossible to directly apply the theory in practice. Then, reasonable approximations are necessary in order to extract focused aspects. Band theory is one of the most successful approximations and has been well applied to semiconductors, which established the current electronics and photonics [3]. On the other hand, various aspects of other materials remain intractable within such simplifications. These kinds of materials are all the more attractive because unexpected and exciting inventions could reside there.

Among such materials, perovskite related transition metal oxides (TMOs) have been intensively studied for many decades, particularly since the finding of high-temperature superconductors [4] because of their diverse and frequently exotic physical properties. Although some of them will be utilized as alternatives to currently used materials, many TMOs are expected to open new fields. Recently, high-temperature superconductors have just started to be applied in a variety of ways directly related to our life [5]. Other TMOs are also under intensive investigations from a variety of viewpoints. Perovskite manganite, for example, shows colossal magnetoresistance and is expected to be used in magnetically operated devices. One of the key materials in perovskite TMOs is $SrTiO_3$, which is the target material in this thesis. This material is located at a contact point between conventional semiconductors and TMOs. The details of $SrTiO_3$ will be mentioned in the

next chapter. We briefly mention the general properties of perovskite materials and the scope of this thesis in the rest of this chapter.

1.2 Carrier doping in perovskite transition metal oxides

The perovskite crystal structure is shown in Fig. 1.1 and the chemical formula is expressed as ABO_3 (A: rare-earth ion or alkali-earth metal, B: transition metal). In spite of this simple structure, the diversity shows up because of the matched combination between A site ions and B site ions, mediated by oxide ions. B site ions determine the basic properties of materials, while A site ions determine the valance of B site ions and the distortion of lattice depending on their radii. Oxide ions constitute the frame of lattice and often mediate the various kinds of interactions. Because carriers have mixed property between localization and itinerancy due to their d-band nature, TMOs are fairly sensitive to external perturbations as well as lattice distortions driven by the substitution of A site ions. In addition, their charges, spins, and anisotropic orbits are all correlated with each other to determine the ground state, which leads to their exotic properties [6].

This fact shows that, in this group of materials, carrier doping is one of the most crucial ways to change their properties and even ground state [7]. The most common way for doping is a chemical substitution of A site ions. In addition, we can sometimes utilize other techniques such as electrostatic field-effect doping [7] and photocarrier doping. As well as other TMOs, carrier doping plays an important role in $SrTiO_3$. As will be mentioned in the next section, we studied photoconductivity of $SrTiO_3$ because of its unique way for carrier doping.

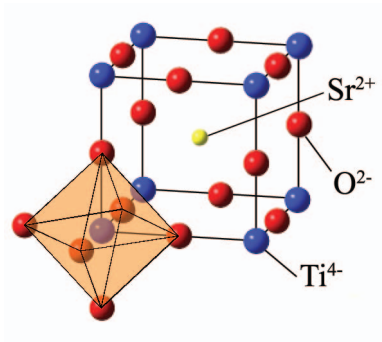

Figure 1.1: Cubic perovskite structure. Indicated ions represent the case of $SrTiO_3$. Titanium ions are octahedrally coordinated, while strontium ions fill vacant spaces between the octahedra.

1.3 Scope of this thesis

The aim of this thesis is to characterize the transport properties of $SrTiO_3$ under ultraviolet illumination. As briefly mentioned above, $SrTiO_3$ can connect oxide materials with conventional semiconductors because of its high mobility exceeding 10^4 cm^2 V^{-1} s^{-1} [8], which is rather exceptional among oxide materials. The eventual goal is the realization of two-dimensional electron gas (2DEG) in $SrTiO_3$, utilizing the photoconductivity. Although extremely clean two-dimensional electron gas can be obtained in conventional semiconductors such as Si and GaAs [9], $SrTiO_3$ is rather distinctive in several points. First of all, this material is highly ionic rather than covalent. Secondly, the dielectric constant of $SrTiO_3$ is extraordinary large because of the suppressed ferroelectric transition by quantum fluctuations [10]. As well as the large effective mass, the strongly polarizable lattice of $SrTiO_3$ could make a difference in various interactions affecting electronic states. Thirdly, $SrTiO_3$ shows superconductivity below 1 K [11]. The coexistence of superconductivity and 2DEG is another interesting issue.

For the purpose, two kinds of techniques must be fulfilled: Carrier doping and their confinement. Conventionally, these conditions have been satisfied either by field-effect doping in metal-oxide-semiconductor structures [12] or by modulation doping at the heterointerface [13]. In the case of $SrTiO_3$, field-effect doping has recently been studied and some results showed it is close to the realization [14, 15]. Photocarrier doping was also utilized to adjust the carrier density but played a minor role in conventional semiconductors [16]. On the other hand, in the case of $SrTiO_3$, photocarrier doping can effectively be utilized because any complicated structures are not needed and we can avoid the effect of degraded surface structure mainly caused by its ionic nature and high dielectric constant [17, 18].

There is another aspect to study photoconductivity of $SrTiO_3$. Recently, it has been demonstrated that photocarrier was injected to oxide thin films grown on $SrTiO_3$ substrates, which shows potential applicability of this phenomenon [19]. Because the field of oxide heterointerfaces is still an emerging area often exhibiting exotic properties [20], some new phenomena can be expected in photonic responses there. Our study can be a basis for such photoinduced phenomena in the field of oxide materials.

Chapter 2

Physical properties of $SrTiO_3$

In this chapter, we survey the physical properties of $SrTiO_3$, which covers almost all basic properties except magnetism. Nondoped $SrTiO_3$ is a insulator and the resistivity at room temperature is above 10^{13} Ω cm [21] with a wide band gap of 3.2 eV [22] between the $2p$ band of oxygen and the $3d$ band of titanium. Substitution of La at the Sr site, Nb at the Ti site, or oxygen vacancies produce mobile electrons and 0.1 at % doping is enough to create a metallic state with the maximum mobility exceeding 10^4 cm^2 V^{-1} s^{-1} at low temperature [8,23,24] as shown in Fig. 2.1. Further doping around 1 at % develops a superconducting phase below 0.5 K [25,26]. The crystal structure of $SrTiO_3$ is cubic at

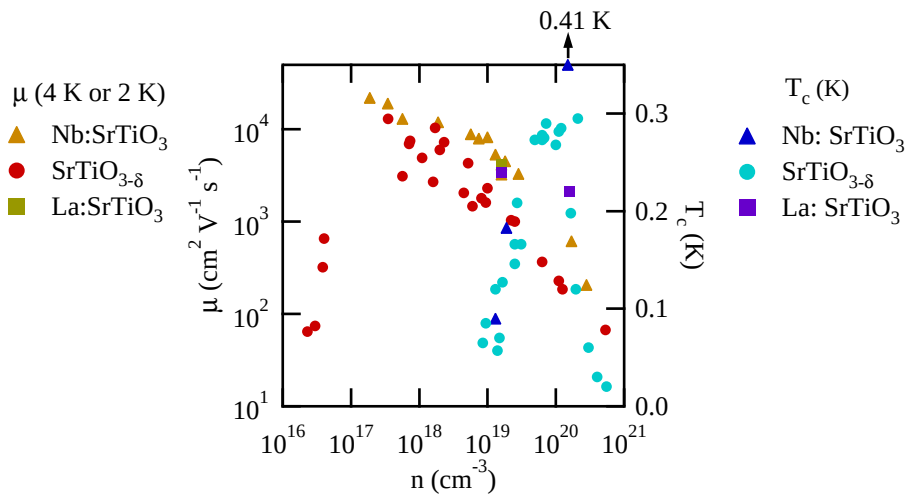

Figure 2.1: Mobility (μ) at liquid helium temperature and superconducting transition temperature (T_c) as a function of carrier density. References for μ are from [8, 23, 24], while T_c are from [25, 26].

room temperature and goes through a cubic-tetragonal structural transition at around 110 K as shown in Fig. 2.2 [27]. The relative permittivity follows a Curie-Weiss law down to 50 K and reaches a maximum value exceeding 10^4 around 5 K [28]. Below 5 K, the permittivity remains constant because the classically expected ferroelectric transition

is suppressed by quantum fluctuations (zero point motion of oxygen) [10]. Below, we explains the underlying electronic and phonon structures. We also introduce some of the outstanding resultant properties.

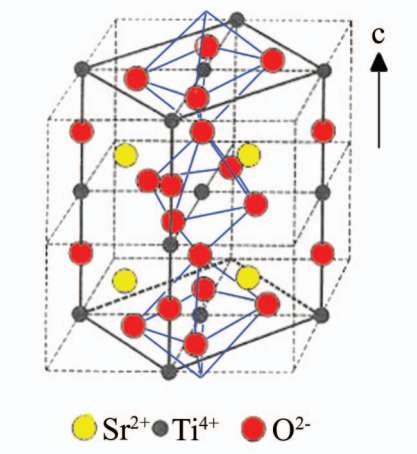

Figure 2.2: Tetragonal lattice of $SrTiO_3$ below 110 K. The oxygen octahedra alternately rotate along the c axis. The figure (modified) is from T. Sakudo, H. Unoki, Phase transition (110°K) and lattice dynamics in strontium titanate, Kotai Butsuri **4**, 3 (1969).

2.1 Band structure

Band structure is the most fundamental information characterizing the electronic transport and optical properties. The Fermi surface of $SrTiO_3$ is experimentally determined mainly by galvanomagnetic oscillation [29–31] in comparison with the band calculations [32–34]. Magnetoresistance [35–37], piezoresistance [38], optical absorption [39–41], tunneling spectroscopy [42], and interband raman scattering [43] were also used to support the previous reports. The band structure of $SrTiO_3$ was intensively studied and a number of controversies were invoked due to the multidomain structure caused by the tetragonal distortion at 110 K [44], which obscures proper interpretations in addition to discrepancies among band calculations.

The band structure was initially calculated by A. H. Kahn *et al.* [32]. According to their results, the conduction band consists of a titanium t_{2g} band, while the valance band consists of a oxygen $2p$ band with a large band gap. Their result showed that the conduction band minimum is located at the X point while valence band maximum is located at the Γ point as shown in Fig. 2.3. Many experimental results supported the calculation of many-valley model including optical absorption [39–41], low-field magnetoresistance (MR) [35, 36], and Shubnikov–de Haas (SdH) oscillation studies [29]. A few other possibilities were also suggested [38].

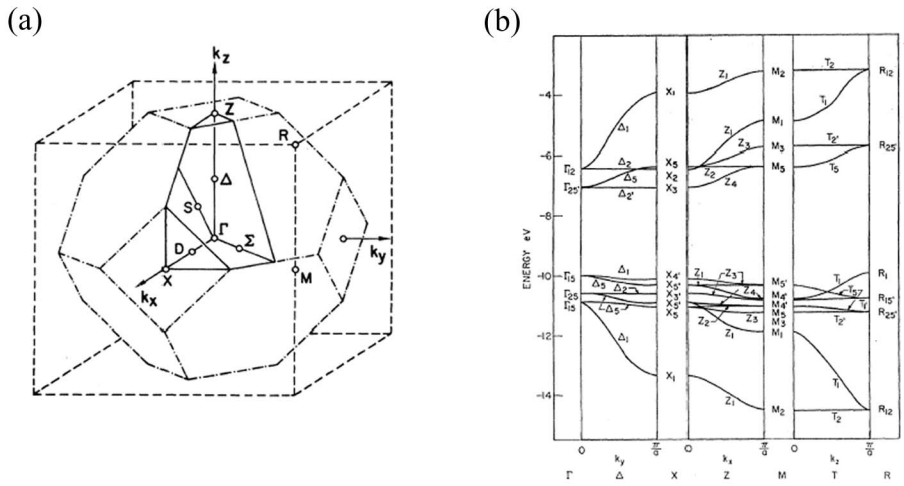

Figure 2.3: (a) Brillouin zone for the body-centered tetragonal Bravais lattice (Ref. [34]). In the case of cubic structure, Z point is equivalent to X and D line is equivalent to Δ. (b) Band structure of $SrTiO_3$ calculated by Kahn *et al.* [32].

In 1972, L. F. Mattheiss suggested a new result of band calculation fitting optical and cyclotron mass measurements [33], which indicated that the conduction bottom is located at Γ as shown in Fig. 2.4 (a). They also calculated the effect of the cubic-tetragonal transition, which showed that one of the three-fold degenerate t_{2g} bands are split by the tetragonal distortion, and the degeneracy of the remaining two-fold bands is lifted by the spin-orbit interaction as shown Fig. 2.4 (b) [34]. With the carrier density of 10^{19} cm^{-3}, the two lowest bands are partially filled in the cubic phase (Fig. 2.5 (a)), while only the outer Fermi surface is present at Γ in the tetragonal phase due to the enhanced spin-orbit split gap (Fig. 2.5 (b)). These results triggered a lot of renewed experiments to reconsider previous work. Fortunately, a technique to obtain a monodomain $SrTiO_3$ was invented so that precise investigation of Fermi surface became feasible [45]. The subsequent experiments of low-field MR [37], magnetothermal oscillation [30], and SdH oscillation studies [31] confirmed that the many-valley bands are not compatible with their results and supported the warped model. In the previous studies before the band calculation by Mattheiss, their claim was that the results were inconsistent with a single band at Γ but they did not exclude a possibility of double bands at Γ. The newer experiments concluded that the many-valley model was inconsistent and the warped model was consistent with their results.

In spite of the qualitative correspondence between the newer experiments and the calculation by Mattheiss, there are a few discrepancies in detail, which is shown in Fig. 2.5 as the Fermi surface along the [001] direction. Firstly, the outer Fermi surface is highly anisotropic extending in the X direction in the calculation [34], while it is some-

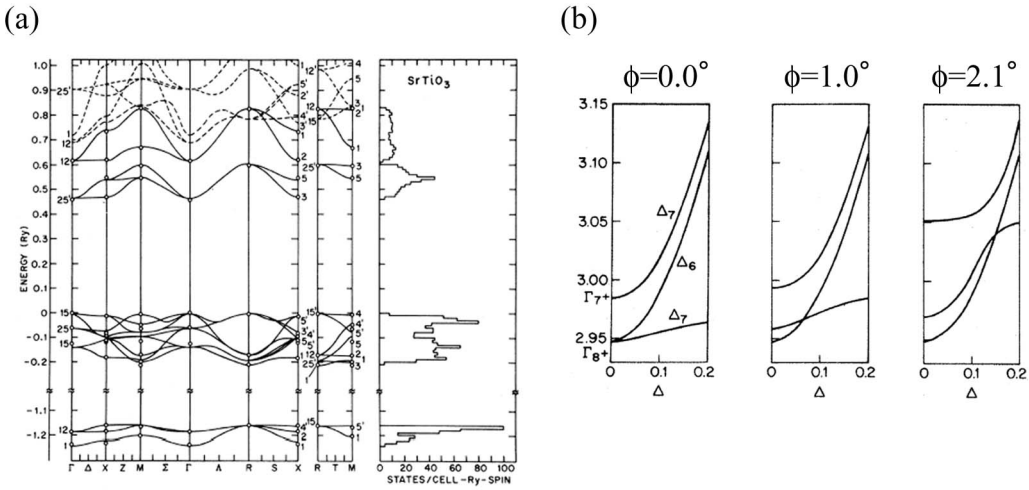

Figure 2.4: (a) Band calculation of $SrTiO_3$ by Mattheiss [33] and (b) the effect of tetragonal distortion including the spin-orbit interaction [34]. ϕ is the angle of octahedral rotation and 2.1° is the value at 4.2 K [27].

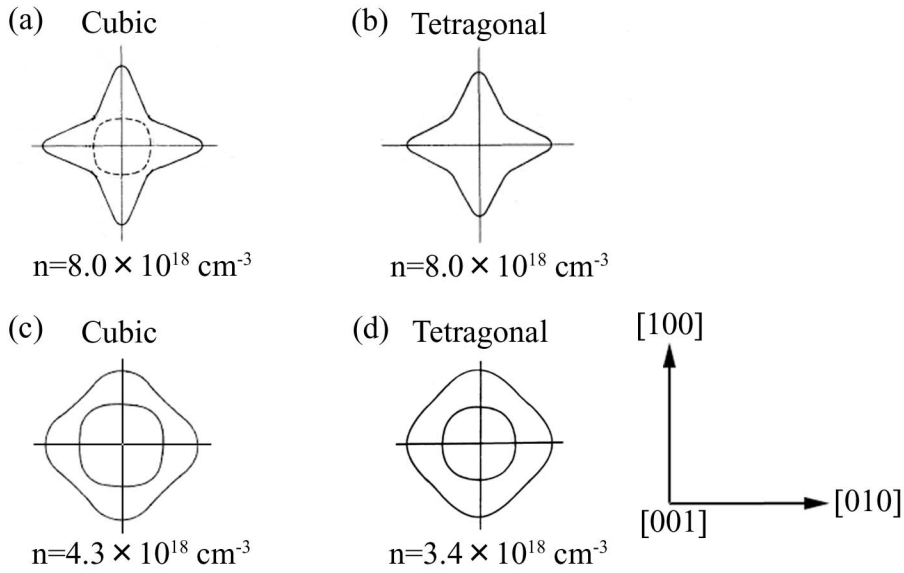

Figure 2.5: Calculated Fermi surface by Mattheiss in (a) cubic phase and (b) tetragonal phase [34]. (c) Fermi surface estimated from MR measurement in cubic phase [37]. (d) Fermi surface estimated from SdH measurement in tetragonal phase [31]. Carrier density of each Fermi surface is indicated in the figure. All Fermi surfaces are in the (001) plane.

what rounded from the experiments of magnetothermal and SdH oscillations [30, 31, 37]. Secondly, different values were estimated for the gap caused by the spin-orbit interaction. The gap was calculated to be about 20.7 meV in the tetragonal phase [34], while the experimental value from interband electronic Raman scattering was 1.54 meV [43]. Irrespective of the quantitative agreement, the observation of two components in SdH oscillation suggests the overestimation of the spin-orbit interaction in the calculation.

Although the valence band top is located at Γ in both calculations [33], experimental results of optical absorption suggested that the band gap is indirect [41, 41]. As pointed out by Mattheiss, however, the energies of valance bands at Γ, R, and M are almost degenerate and it is difficult claim where the valence band maximum is located both from the calculation [33] and the measurements at present.

2.2 Phonon structure and related properties

The phonon structure plays a crucial role for many outstanding properties of $SrTiO_3$ such as the high electron mobility, superconductivity, and photosensitivity, although some aspects are still controversial. There are two kinds of transverse optical (TO) soft phonons, which can be explained by Cochran's theory of ferroelectricity [46]. They claim that displacive structural transitions take place when Coulomb forces become equal to short-range forces and the frequency of TO modes is expressed as

$$\hbar\omega_{\mathrm{TO}}^2(\boldsymbol{k}) = K(T - T_{\mathrm{C}}), \tag{2.1}$$

where K is a constant, T is the temperature, and T_{C} is the transition temperature. In the case of $SrTiO_3$, one type of soft phonons at the R point is condensed at 110 K, while another type at Γ is condensed below 0 K.

In real space, the transition at 110 K corresponds to the tetragonal structural distortion, as pointed out by P. A. Fleury *et al.* [47]. Because the soft phonons at R point are turned to the Γ point below T_{C} due to the doubling of the unit cell, it was observed (by Raman scattering [47] and neutron scattering [48]) that the condensed phonons appear at Γ as temperature decreases, as shown in Fig. 2.6. However, the structural change is so small that its effect on the electronic structure can be rarely probed [49]. On the other hand, the softened TO phonons correlates with the acoustic phonons at the zone center, giving rise to, for example, the anomalous peak in ultrasonic attenuation [50].

The soft TO phonons at the zone center are not completely soften because of quantum fluctuations. The softening and its deviation from Curie-Weiss law have been observed by neutron scattering as shown in Fig. 2.7 (a) [51]. In contrast with the soft phonons at the R point, this mode strongly affects the dielectric constant (Fig. 2.7 [51] (b)) [28]

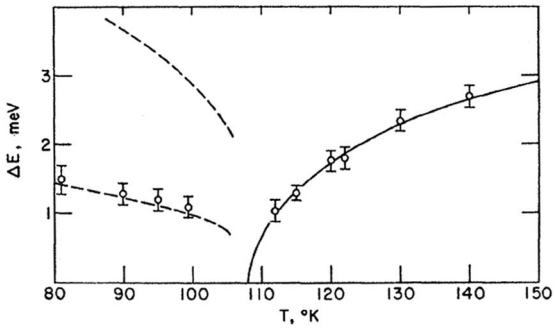

Figure 2.6: The result of neutron scattering about the TO phonons of $SrTiO_3$ around the cubic-tetragonal structural transition temperature. Solid line and broken line indicate the energy of TO phonons observed at R point and Γ point, respectively. Above T_C, this mode is doubly degenerate and split into two kinds of phonons by the symmetry lowering. From Ref. [48].

through the Lyddane-Sachs-Teller relation

$$\frac{\epsilon_0}{\epsilon_\infty} = \frac{\prod_i \omega_{i\mathrm{LO}}^2(0)}{\prod_i \omega_{i\mathrm{TO}}^2(0)}, \tag{2.2}$$

where ϵ_0 and ϵ_∞ are the dielectric constant at the zero and infinite frequencies, respectively, and $\omega_{i\mathrm{TO}}(0)$ and $\omega_{i\mathrm{LO}}(0)$ are the frequencies of transverse optical and longitudinal optical modes of the i branch at $\boldsymbol{k} = 0$. This anomalous dielectric behavior gives the high mobility and perhaps high photosensitivity in $SrTiO_3$.

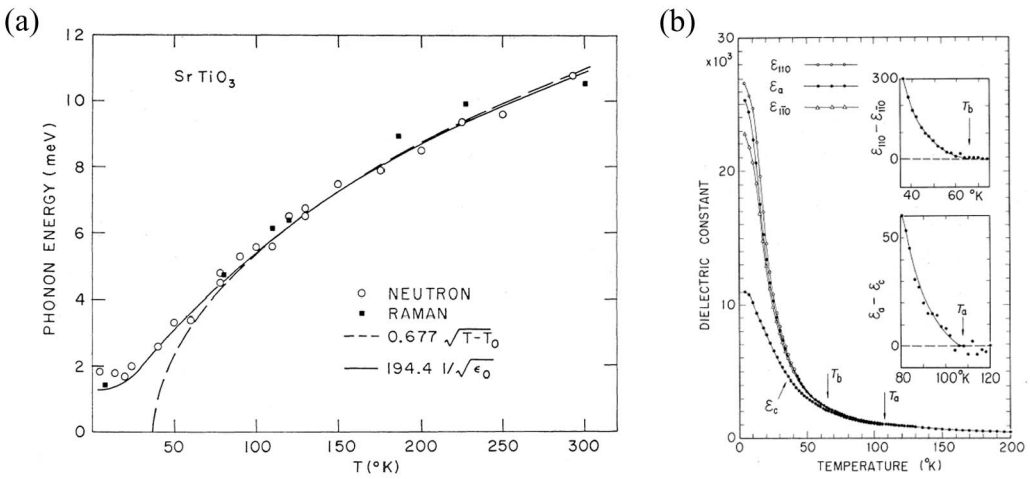

Figure 2.7: (a) The energy of the TO soft phonons at the zone center measured by neutron scattering and scattering. From Ref. [51]. (b) The dielectric constant of $SrTiO_3$. From Ref. [28]. They are connected by Lyddane-Sachs-Teller relation in the framework of the Cochran's theory.

2.3 Superconductivity

Superconductivity in a semiconductor does not seem probable based on the theory of superconductivity by Bardeen, Cooper, and Schrieffer [52] , which predicts

$$kT_c = \hbar\omega \exp\left[-\frac{1}{N(0)V}\right], \tag{2.3}$$

where k is the Boltzmann constant, T_c is the superconducting transition temperature, $\hbar$ is the Planck constant divided by 2π, ω is the phonon frequency involved, $N(0)$ is the density of states at the Fermi level, and V is the strength of the coupling between electrons and phonons. Because $N(0)$ of doped semiconductors is usually several orders of magnitude smaller than metals, in order to obtain superconductivity in a feasible temperature range, assuming a similar phonon frequency, V should be fairly large to compensate the small value of $N(0)$. M. L. Cohen proposed the possibility of superconductivity in many-valley degenerate semiconductors [53] and it was found in a number of semiconductors such as GeTe [54] and Si [55].

Along with such semiconductors, the superconductivity of $SrTiO_3$ was found [11] and explained explained by Cohen's theory [25]. However, since the conduction band bottom seems to be located at the zone center, as mentioned above, this theory cannot be applied to the case of $SrTiO_3$. Therefore other mechanisms were proposed such as theories mediated by a soft optical phonon [56], two TO phonons [57], and plasmons [58]. However, this is not resolved yet.

2.4 Photoconductivity

Photoconductivity is one of the most characteristic properties of semiconductors [59]. Although $SrTiO_3$ shows the large photoconductivity, only a small number of studies on the photoconductivity of $SrTiO_3$ have been reported, compared with other properties of $SrTiO_3$ such as the electronic and phonon structure. H. Yasunaga obtained the mobility of photocarrier-doped $SrTiO_3$ for the first time and found high mobility as shown in Fig. 2.8 (a) [60], which is compared with the chemically doped case (b). Several groups utilized the photoconductivity in order to probe the in-gap states often combined with photoluminescence [21]. Recently, the large enhancement of dielectric constant of $SrTiO_3$ has been observed under ultraviolet illumination and small electric field [61]. Although the origin is not clear yet, several renewed studies were inspired in order to investigate its relation with the photoconductivity [62].

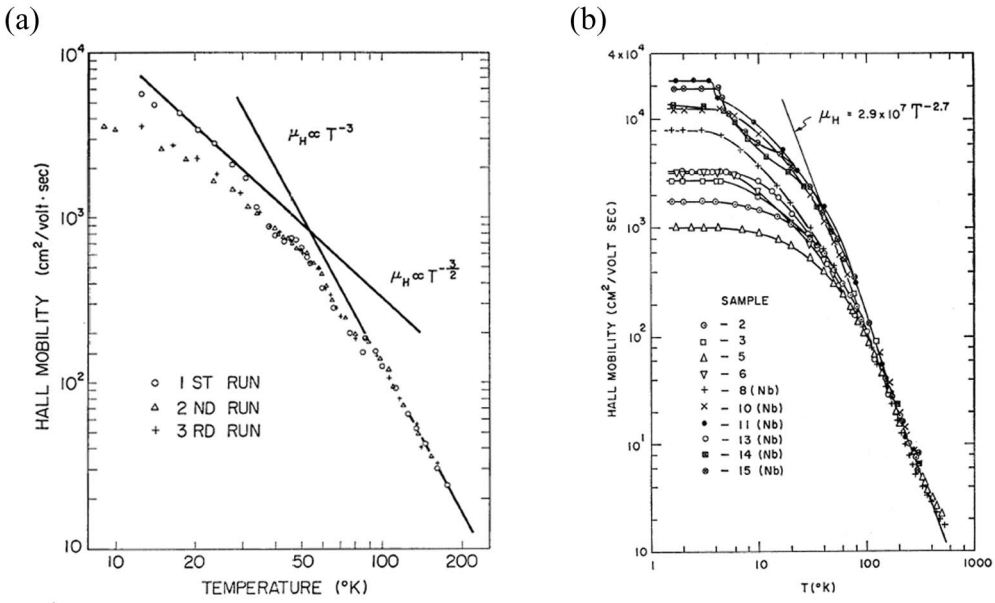

Figure 2.8: Mobilities of $SrTiO_3$ as a function of temperature (a) under illumination from Ref. [60] and in the chemically doped case from Ref. [8].

Chapter 3

Equipment and techniques

$SrTiO_3$ single crystals used for the measurements of photoconductivity were purchased from either Furuuchi Chemical Co. or Shinkosha Co. and $SrTiO_3$ thin films were fabricated by pulsed laser deposition (PLD). The thin films were characterized by atomic force microscopy (AFM) (Nanoscope IV, Veeco Instruments Inc.) and x-ray diffraction (XRD) (Discover 8, Bruker AXS Inc.). The thickness of the films were estimated by a stylus profilometer, reflection high energy electron refraction (RHEED) oscillations, or fringes in XRD if necessary. The transport measurement was carried out in a Physical Properties Measurement System (PPMS) (Quantum Design Co.) and 100 W Xe source (LAX-102, Asahi Spectra Co.) was employed to illuminate samples. We will briefly explain each technique in this chapter.

3.1 X-ray diffraction

XRD is a widely use method to determine the structure of molecules and solids. In particular, this is used for solid crystals because the wavelength of x-rays is typically a similar order as the atomic spacing. We can detect the intense interference of diffracted x-rays from the periodically arranged atoms.

The intensity profile of the diffracted x-rays is related to the reciprocal lattice, which is the Fourier transform of the lattice in real space. As shown in Fig. 3.1, the Ewald sphere is defined as a sphere whose radius is the amplitude of the incident x-ray wavevector and whose center is located at the origin of the incident wavevector. When the Ewald sphere intersects with any reciprocal lattice points, we obtain diffracted x-rays in the direction of the corresponding reciprocal vector extended from the sample; that is,

$$\boldsymbol{q} = \boldsymbol{k}_s - \boldsymbol{k}_i, \tag{3.1}$$

where $\boldsymbol{q}$ is any vector extended from one point to another on the Ewald sphere, $\boldsymbol{k}_i$ is the incident wavevector, and $\boldsymbol{k}_s$ is the scattered wavevector. The intensity of diffraction is

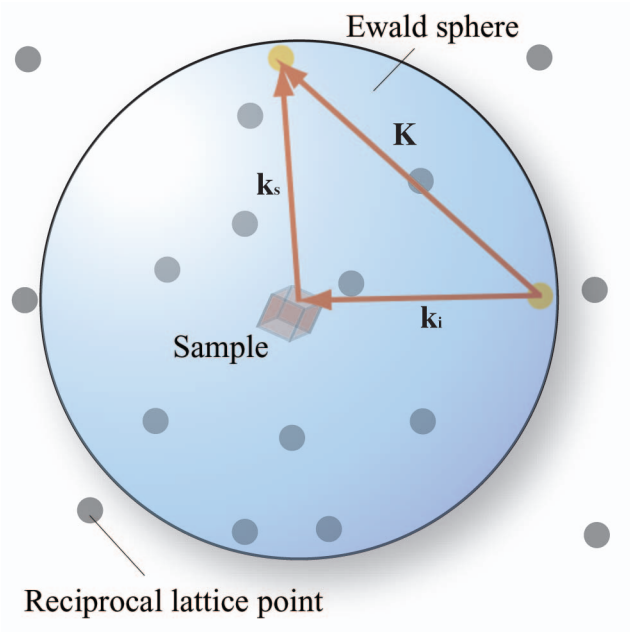

Figure 3.1: Schematic diagram of x-ray scattering in reciprocal space. $\boldsymbol{k}_i$ is the incident wavevector, $\boldsymbol{k}_s$ is the scattered wavevector, and $\boldsymbol{K}$ is the scattering vector. $\boldsymbol{K}$ connects two reciprocal lattice points on the Ewald sphere.

expressed as

$$I(\boldsymbol{q}) = |f(\boldsymbol{q})|^2 \cdot |L_x(q_a)|^2 \cdot |L_y(q_b)|^2 \cdot |L_z(q_c)|^2, \tag{3.2a}$$

$$f(\boldsymbol{q}) = \int_{\text{unit cell}} \rho(\boldsymbol{r}) e^{-2\pi i \boldsymbol{q}\cdot\boldsymbol{r}} \mathrm{d}\boldsymbol{r}, \tag{3.2b}$$

$$\begin{aligned} L_x(q_a) &= e^{-\pi i (N_x - 1) q_a d_{hlk}} \frac{\sin \pi N_x q_a d_{hlk}}{\sin \pi q_a d_{hlk}}, \\ L_y(q_b) &= (x \to y, \quad a \to b), \qquad L_z(q_c) = (x \to z, \quad a \to c), \end{aligned} \tag{3.2c}$$

where x, y, and z represent the directions of three principal axes in real space, a, b, and c represent the directions of the three principal axes in reciprocal space, $\boldsymbol{r}$ is the coordinate in real space, $\rho(\boldsymbol{r})$ is the density of electrons at $\boldsymbol{r}$, N_x is the number of unit cells along the x direction, and d_{hlk} is the spacing of $(h\ l\ k)$ planes. $L_x(q_a)$ is called the Laue function and gives the condition of diffraction, Eq. (3.1). $f(\boldsymbol{q})$ depends on the type of atoms and the specific coordination of those atoms in the unit cell, and it determines the intensity of diffraction satisfying Eq. (3.1). When the size of the sample is much larger than the x-ray penetration depth, we can take the limit N_x, N_y, $N_z \to \infty$, and we get $|L_x(q_a)|^2 |L_y(q_b)|^2 |L_z(q_c)|^2 \to \delta(\boldsymbol{q} - \boldsymbol{K})$, where $\boldsymbol{K}$ is the scattering vector, $\boldsymbol{k}_s - \boldsymbol{k}_i$.

When the sample is a thin film, the distinction between planes parallel to and not parallel to the sample surface is important. The diffraction from parallel planes and non-parallel planes is called symmetric reflection and asymmetric reflection, respectively. Figure 3.2 compares the geometries in both cases. In symmetric reflection, we often use

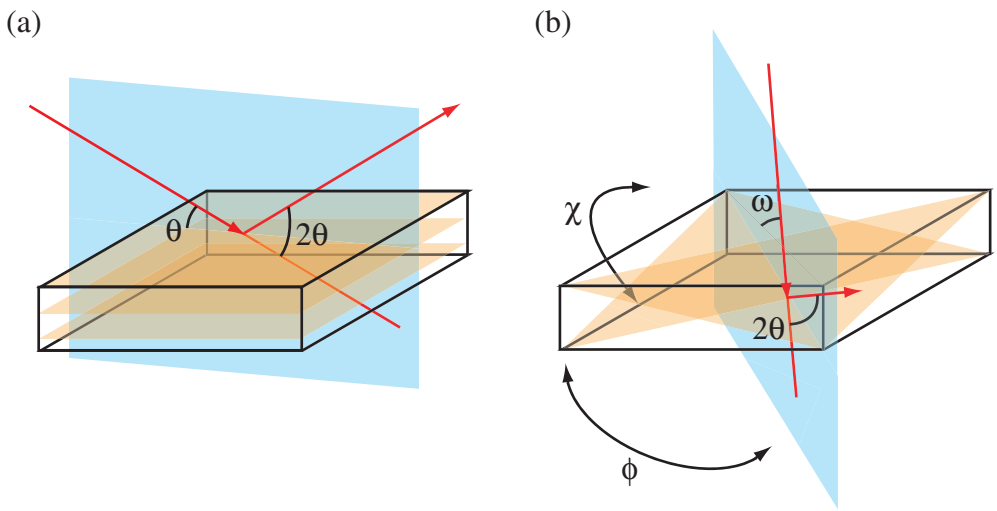

Figure 3.2: Geometries in the measurements of (a) symmetric and (b) asymmetric reflection. Reflection planes are parallel to the sample surface in (a), while not parallel in (b).

θ-2θ measurement, where θ is the incident angle from the (hkl) plane, 2θ is the diffracted angle from incident x-ray direction. If the thin film is epitaxially grown on the substrate, symmetric reflection gives the out-of-plane lattice spacing,

$$d_{hkl} = \frac{n\lambda}{2} \sin\theta \qquad (n\text{: integer}), \tag{3.3}$$

where λ is the x-ray wavelength. On the other hand, in asymmetric reflection, we often measure the intensity two-dimensionally around the peak of diffraction on the Ewald sphere, which is called reciprocal space mapping (RSM) and contains information about the spacings of both out-of-plane and in-plane lattice planes.

Other useful information than the lattice spacings is the thickness of films derived from fringes near a Bragg peak in the θ-2θ measurement, which is

$$t = \frac{\lambda}{2(\sin\theta_1 - \sin\theta_2)}, \tag{3.4}$$

where $\sin\theta_1$ and $\sin\theta_2$ are neighboring angles which give zero value of the Laue function with finite N. Moreover, the broadening of peaks in a reciprocal space map gives information about mosaicity and the rough size of grains, which we do not discuss here.

3.2 Pulsed laser deposition

PLD is a quite powerful method to deposit complex oxide thin films and multilayered structures, because of its simplicity and versatility. Films are grown by ablating a bulk compound usually by ultraviolet pulsed laser with a typical pulse duration of 20 ns (for

excimer lasers). Generally, PLD has three steps to constitute materials on the substrate: vaporization of the target material, transport of the vapor plume, and reconstruction of the growing film. Films are grown through thousands of repetitions of these steps [63].

Our chamber system used in this study consists of a load-lock chamber and a main chamber. The chambers are evacuated by turbo pumps following rotary pumps and the base pressure of the main chamber is kept around 10^{-8} Torr. Thermodynamically, substrate temperature and oxygen pressure are the most important parameters to control thin film growth. A nickel plate was used as a substrate holder and heated by a infrared laser. The temperature was measured by a pyrometer because the temperature of the substrate surface must be precisely controlled. The oxygen pressure of the main chamber was manually adjusted by controlling the rate oxygen injection and measured by an ion gauge. The film growth was monitored by RHEED oscillation if necessary, which will be explained in the next section.

3.3 Reflection high energy electron refraction

RHEED is an indispensable tool for the fabrication of multilayered structures and is even useful for the deposition of single layer films because the pattern of spots and oscillations contains a lot of information related with, for example, surface structure, deposition rate, and lattice relaxation. We will explain the first two topics [64].

3.3.1 RHEED spot pattern

RHEED is usually used in the geometry of grazing incidence, which is why RHEED is sensitive to the condition of the surface. Although the principle is based on the description in reciprocal space and similar to x-ray diffraction, reciprocal points become reciprocal rods in two dimensions along the direction normal to the surface ($N_z \to 1$ in Eq. (3.2c)), giving diffraction spots of the two-dimensional lattice as shown in Fig. 3.3. In addition, because the wavevector is relativistically expressed as

$$k = \frac{1}{\hbar}\sqrt{2mE + \frac{E^2}{c^2}}, \tag{3.5}$$

$k = 785$ nm^{-1} when $E = 20$ keV, where $\hbar$ is the Planck constant divided by 2π, m is the mass of an electron, E is the energy of an electron, c is the speed of light. Taking into consideration that the lattice constant of the reciprocal unit cell of $SrTiO_3$ is 2.56 nm^{-1}, the radius of the Ewald sphere of electrons is much larger. Due to finite the size of the samples or inevitable imperfections of the lattice, the radii of these rods are ideally zero but often have finite value and therefore the spots tend to become streaks.

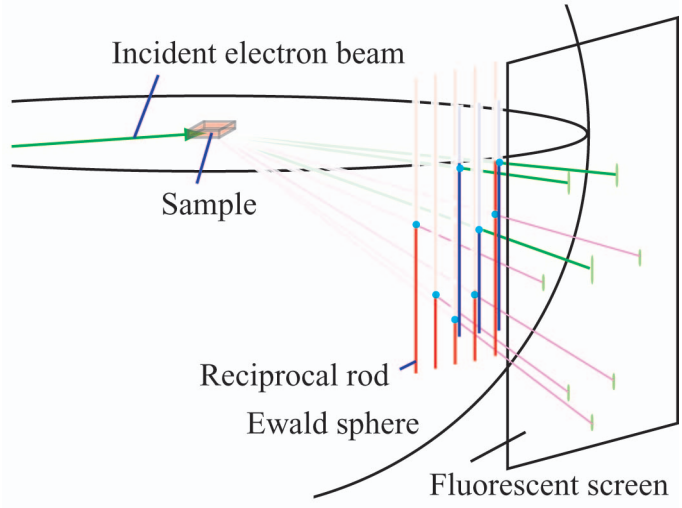

Figure 3.3: Schematic diagram of the geometry of RHEED. RHEED spots appears in the direction of intersections between the Ewald sphere and the reciprocal lattice rods. Red reciprocal rods give zeroth order diffraction, while blue rods give first order diffraction.

3.3.2 RHEED oscillation

Temporal variation of the RHEED intensity is strongly related to the roughness of the surface. Figure 3.4 shows schematic diagram of variation of RHEED intensity depending on the morphology of growth. When adatoms tend to nucleate three-dimensionally, the RHEED intensity rapidly decreases as shown in Fig. 3.4 (a). On the other hand, the RHEED intensity remains high and recovers responding to each pulse when adatoms have considerably mobility to reach the most stable position as shown in Fig. 3.4 (c). RHEED oscillation is only observed when nucleation starts after the completion of one monolayer as shown in Fig. 3.4 (b). In this case, one oscillation corresponds to the growth of one monolayer, and this growth mode has been utilized to precisely control the fabrication of multilayered structures. However, exact analysis of observed damping and phase of the oscillation is difficult because they depend on many factors such as the condition of the sample surface (roughness, inhomogeneity, atmosphere around the sample), geometry (incident and azimuth angles), as well as the details of the image acquisition process.

3.4 Photoconductivity measurement

Photoconductivity measurements were carried out down to 2 K and under the maximum magnetic field of 14 T in a PPMS. As shown in Fig. 3.5, the irradiated light from a Xe lamp is bounced by coated mirrors, which cut infrared to avoid heating. Then the light was attenuated by a variable neutral density filter, which changes the intensity

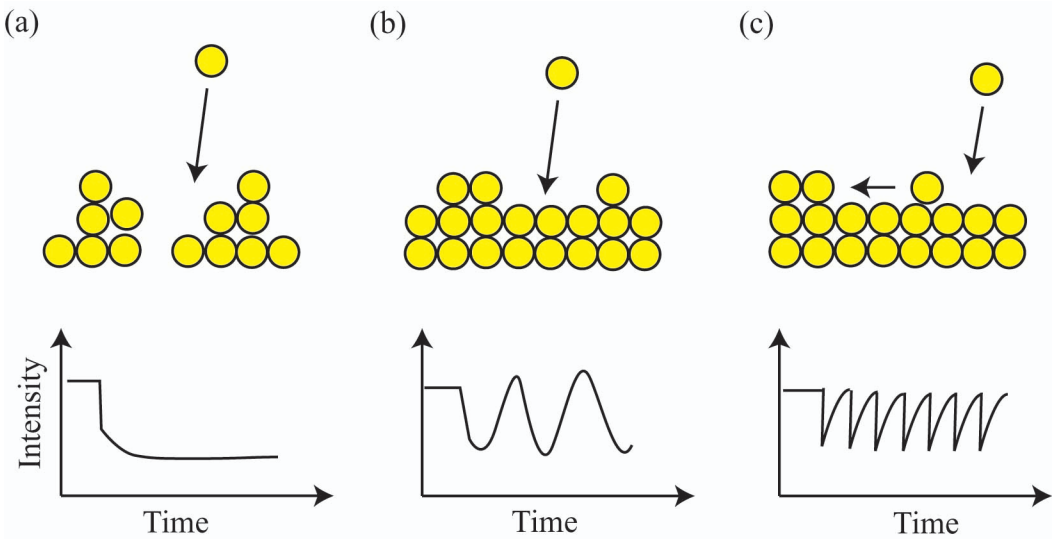

Figure 3.4: Schematic diagram of the types of growth and corresponding RHEED oscillation. (a) Three-dimensional growth, (b) layer-by-layer growth, and (c) step-flow growth.

nominally from 100 % to 5 %, and the other filters at constant rates of 12 % and 1 % if necessary. Subsequently, the light is monochromatized by a band-pass filter with the bandwidth of about 10 nm. We used eight bandpass filters covering every 10 nm from 310 nm to 380 nm. A fiber bundle is glued in a stainless pipe, which is sealed by a Wilson seal at the top of the PPMS. Eventually, the light is imaged on samples by a lens system to give a 2×2 cm^2 square area of uniform illumination. The distance between the lens system and the sample surface is about 8 cm. Under this condition, the maximum intensity we obtained is about 1 mW/cm^2 on the sample surface. Without any bandpass filters, we obtained about ten times more intense light, but heating increased the base temperature up to about 10 K.

In advance of the measurements, we carried out the calibration of the incident light intensity as shown in Fig. 3.6, which is applicable for each wavelength from 310 nm to 380 nm. The absolute value of 100 on the longitudinal axis corresponds to about 1 mW/cm^2 for 380 nm and it almost linearly decreases to about 0.4 mW/cm^2 with decreasing the wavelength to 310 nm. The measured values deviate from nominal values below 50 % of the variable ND filters. We use the measured relative intensity throughout this thesis.

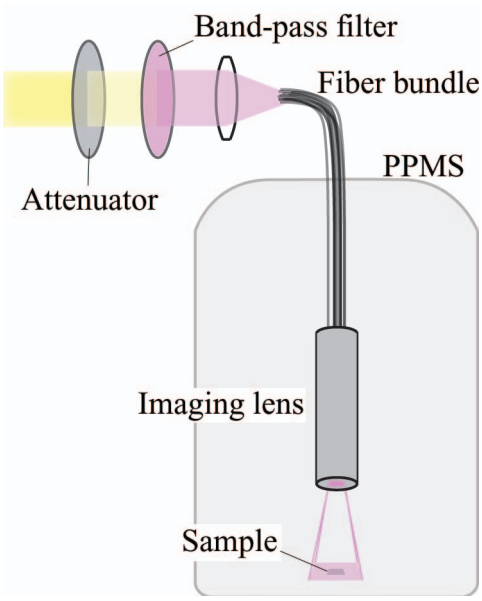

Figure 3.5: Optical system used in the photoconductivity measurements.

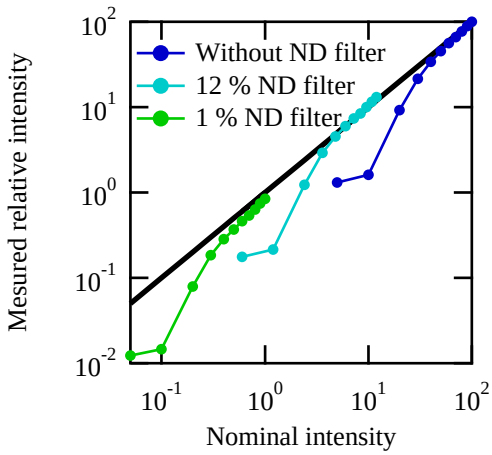

Figure 3.6: Calibration of the light intensity. The value of 100 on the longitudinal axis corresponds to about 1 mW/cm^2. Each point in the graph correspond to the nominal value of the variable ND filter of 5, 10, 20, 30, 40, 50, 60, 70, 80, 90, 100 % from the left.

Chapter 4

Temperature dependence of photoconductivity in $SrTiO_3$ single crystals

4.1 Introduction

As mentioned in Chapter 2, high mobility electron close to 10^4 cm^2 V^{-1} s^{-1} was reported at low temperature in photocarrier-doped $SrTiO_3$ [60], which is advantageous for coherent conduction and photonic operation in oxide heterostructures. Although there are some reports on the photoconductivity, only few focused on the photoconducting properties and magnetotransport response.

In this study, we have investigated the photoconductivity and Hall coefficient with various wavelength and intensity of illumination as a function of temperature. As a result, we found extremely high mobility at low temperature as reported by Yasunaga [60]. In spite of the fact that a sample dependence were observed in the carrier density, such high mobility was robust and almost independent of samples in the low temperature limit. Although we did not carry out any measurements to determine the microscopic origins of the sample dependence, we will mention the possible factors suggested by other reports. This study can be a foundation for any measurements related to photoresponse such as the subsequent studies on low-temperature magnetotransport properties.

4.2 Experimental

We purchased $SrTiO_3$ single crystals from Furuuchi Chemical Co. (Furuuchi) and Shinkosha Co. (Shinkosha). The surface of crystals from Furuuchi is polished to an optical grade, while the surface of crystals from Shinkosha is polished and etched by buffered HF. We used a PPMS to cool down and measure the photoresponse of samples. For high resistance measurements, we used a sourcemeter (Model 2410, Keithley) instead

of the resistance bridge installed in the PPMS.

4.3 Results and discussions

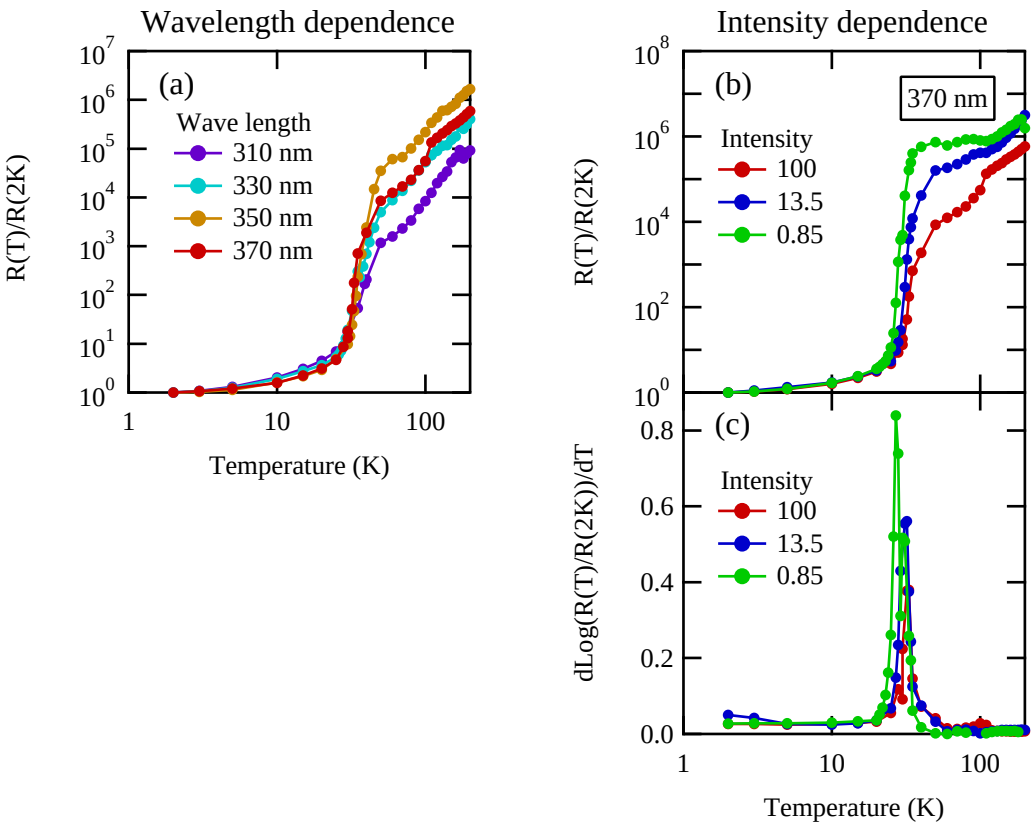

Figure 4.1: (a) Normalized resistance as a function of temperature under different wavelengths of illumination, and (b) under different intensities with fixed wavelength of 370 nm. (c) Derivative of curves in (b). All data are normalized by the values at 2 K in (a) and (b). Samples are from Shinkosha.

Figure 4.1 (a) and (b) shows sheet resistance under illumination of different wavelength and intensity as a function of temperature, which is normalized by the value at 2 K because the attenuation rates of ND filters are slightly dependent on wavelength. In addition, we found that it is difficult to obtain reproducible values even under the same intensity and wavelength of illumination once we take out samples from the dewar of a PPMS. As shown in Fig. 4.1 (a), almost independent of wavelength, we observed a sharp change in resistance around 30 K, while (b) shows that temperature dependence is qualitatively the same under different intensity but shows a slight dependence. The difference in the resistance with different wavelength in Fig. 4.1 (a) probably originates from a wavelength dependence of the mobility at low temperature as will be discussed in

Chapter 5 and this is absent at high temperature. In order to see the intensity dependent effect clearly, we took derivatives of the curves in Fig. 4.1 (b) as shown in Fig. 4.1 (c), This indicates that, as the intensity decreases, the change in resistance around 30 K becomes sharper and the peak value of the derivative is also shifted to lower temperature. A qualitatively similar behavior was observed by T. Feng and attributed to the localized trapping center for holes in the band gap [21]. Quantitatively speaking, however, the

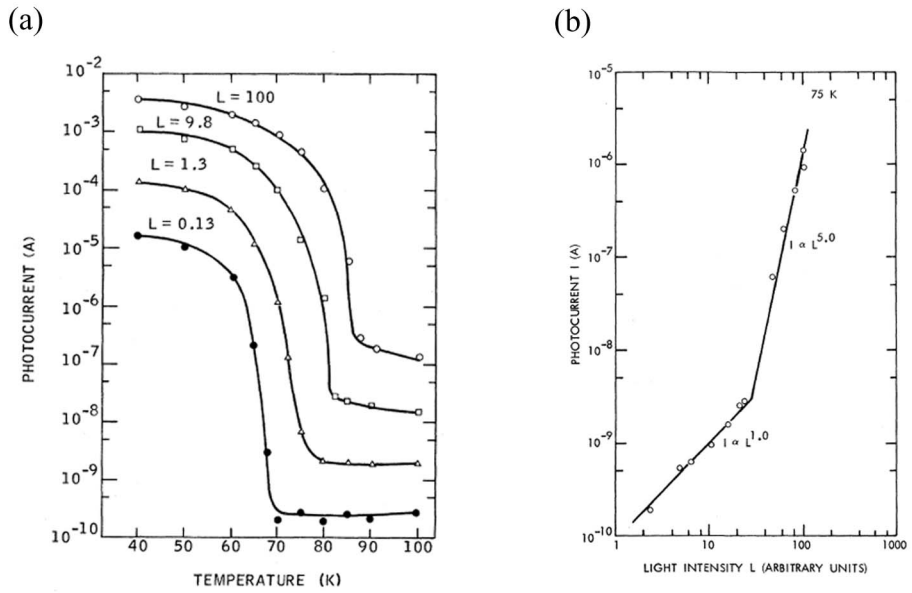

Figure 4.2: (a) Photocarrier variation as a function of temperature for different intensities of excitation (Fig. 4 in Ref. [21]). (b) Photocurrent as a function of excitation intensity at 75 K (Fig. 5 in Ref. [21]). The wavelength is 380 nm and L=100 corresponds to 5×10^{-4} mW/cm^2.

temperature of the sharp change in resistance is more sensitive in their case as shown in Fig. 4.2 (a). This causes superlinearity in photocurrent as a function of excitation intensity as shown in Fig. 4.2 (b). This discrepancy could be because of the different intensity from our measurements. However, when we take into account that the intensity they used is 5×10^{-4} mW/cm^2, which is much weaker than our, we should have observed more sensitive intensity dependence. Another possible reason may be different qualities of samples, which will be discussed later.

We then carried out conductivity and Hall measurements as a function of temperature using two single crystals from different vendors, as shown in Fig. 4.3 under 370 nm illumination. We found a sharp change in conductance as in Fig. 4.1 but at different temperatures dependent on samples. Exactly the same difference can be found in recent reports between Ref. [65] (Furuuchi) and Ref. [62] (Shinkosha). Other reports also observed a similar sharp change in conductance at different temperatures as in Fig. 4.2.

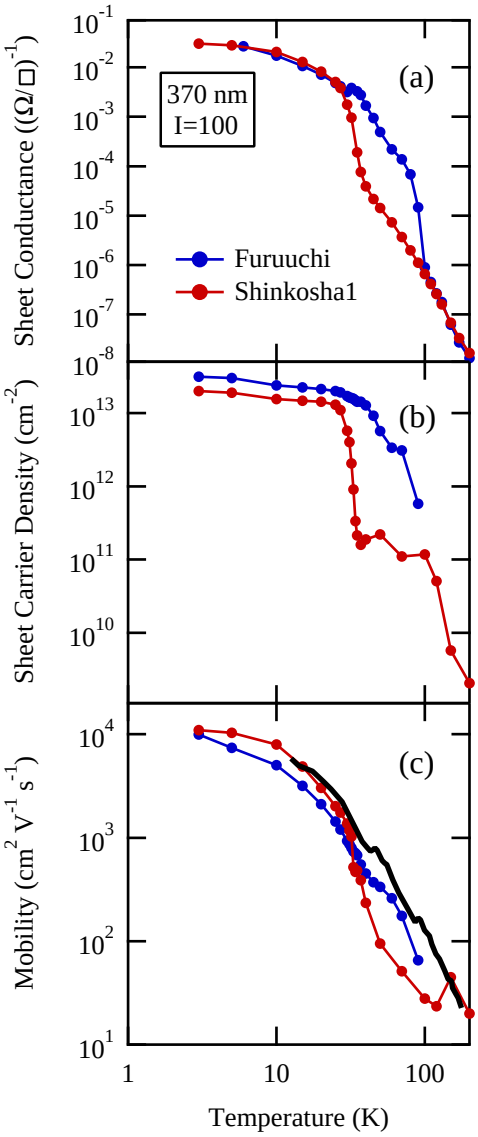

Figure 4.3: (a) Sheet conductance, (b) sheet carrier density, and (c) mobility of different samples under illumination of 370 nm and I=100 as a function of temperature. The solid black curve in (c) is the data from Ref. [60].

Since conductance is expressed, in Drude form, as

$$\sigma = \frac{ne^2\tau}{m^*} = ne\mu, \tag{4.1}$$

there are two possible origins of the change of conductance, that is, n or μ, where n is the carrier density, τ is the scattering time, m^* is the effective mass of a carrier, and μ is the mobility. In order to clarify the origin, we carried out Hall measurement. We found that the carrier type was electron and the contribution to the electronic conduction from holes can be neglected. Although precise Hall measurement is difficult at higher temperature due to high resistance, Fig. 4.3 (b) indicates that the carrier density was changed in a similar way to the conductance, while the mobility was found to smooth vary with temperature, independent of samples. Therefore, we can conclude that the sharp change in conductivity is driven by the change of carrier density. In addition, the temperature dependence of mobility indicates that the nature of carriers is almost the same as in the chemically doped case [8]. Such robust high mobility close to 10^4 cm^2 V^{-1} s^{-1} is quite preferable to study coherent conduction at low temperature.

Now, we discuss the possible microscopic origins of the sharp change in the conductance. The density of photoexcited carriers is expressed as

$$n = G\tau_{\text{life}}, \tag{4.2}$$

where G is the generation rate and τ_{life} is the life time of carriers. Then it is important to determine which caused the change of carrier density between G and τ_{life}. Feng proposed that this change is caused by thermal quenching, which is that trapped holes in localized sensitizing centers are excited to the valence band and the recombination rate increases [21]. They confirmed it by photoluminescence and optical quenching by infrared light. According to their interpretation, the discrepancy among previous reports [21, 60, 61, 65–67] is caused by the sample quality, which results in the different energies of sensitizing trapping states. This is also relevant for the result in Fig. 4.1 because thermal quenching at higher temperature means that the level of the sensitizing trapping states are located near the valence band maximum, which causes insensitivity of thermal quenching to the variation of quasi-Fermi level. Hence, the sharp change in the photoconductivity is driven by the collapse of life time

On the other hand, such extraordinarily large photoconductivity has been observed only below the cubic-tetragonal transition temperature, which could imply the importance of soft phonons at the R point as well as the in-gap trapping state. Because such soft phonons are sensitive to the amount of impurities or environment [68], subtle effects can have a large influence on the photoresponses through the change of phonon structure. However, taking into account that the dielectric behavior and photoconductivity

of $KTaO_3$ are surprisingly similar to $SrTiO_3$ [69, 70], the absence of tetragonal-cubic transition in $KTaO_3$ down to low temperature raises a question whether the existence of cubic-tetragonal transition is a prerequisite for large photoconductivity in such materials.

If we consider the analogy between $SrTiO_3$ and $KTaO_3$, the soft phonon at zone center may be relevant to consider. Müller *et al.* related an anomaly in the EPR spectrum with the transition to a macroscopically coherent quantum state at 37 K, involving the zone-center soft phonons [71]. However, it was claimed that this is caused by the accidental crossing between two kinds of soft phonons [72]. In addition, another experiment by precise XRD measurements indicated that this is just caused by aggressive polishing, which generates antiphase ferroelectric boundaries [73]. The existence of such transitions are still controversial and their correlation is also not yet clear.

4.4 Conclusions

We characterized transport properties of $SrTiO_3$ under illumination as a function of temperature and qualitatively reproduced previous reports. Hall measurement suggested that the quantitative discrepancy among reports originates from the change of carrier density rather than mobility. Such sample independent high mobility is the foundation of our subsequent studies of low-temperature magnetotransport. On the other hand, it is interesting to investigate the microscopic origin of sample dependence and unify the discrepancies among all previous reports.

Chapter 5

Low-temperature magnetoresistance measurement of $SrTiO_3$ single crystals

5.1 Introduction

In this chapter, we will show the results of low-temperature magnetotransport properties of $SrTiO_3$ single crystals in the vicinity of the metal-insulator transition. A metal-insulator transition by Anderson localization has been a longstanding issue and experimentally studied in lightly doped semiconductors. In the case of $SrTiO_{3-\delta}$, the metal-insulator transition has been experimentally reported around the carrier density of 10^{18} cm^{-3} [8, 24]. However, slight reduction easily causes inhomogeneous doping. Moreover, Nb-doped $SrTiO_3$ is metallic with carrier density as low as 10^{17} cm^{-3} [8]. Photocarrier doping may be a suitable way to study the metal-insulator transition because of the uniform doping and the precise tuning of the carrier density [74], although carriers are regarded as nonequilibrium unlike chemical doping unless a persistent photoconductivity is present.

In this study, we mapped out the mobility as a function of carrier density by changing the wavelength and intensity of illumination. Although we found that there is a large distribution in the relation between the carrier density and mobility, we observed a weakly localized behavior such as a negative MR, which is reminiscent of weak localization. However, the negative MR is not quantitatively fit by the rigorous theory of weak localization. We will discuses the possibilities of the discrepancies.

5.2 Anderson localization

The localization of carriers due to disorder was initially proposed by P. W. Anderson [75]. In spite of difficulties to treat a disordered system, E. Abrahams *et al.* made a theoretical

breakthrough in 1979 [76]. They expressed conductance as a function of a sample size L and defined

$$\beta = \frac{\mathrm{d}\ln g}{\mathrm{d}\ln L}, \qquad \left(g = \frac{G(L)}{e^2/\hbar}\right) \tag{5.1}$$

where G is the conductance. They assumed that β is dependent on only g and calculated

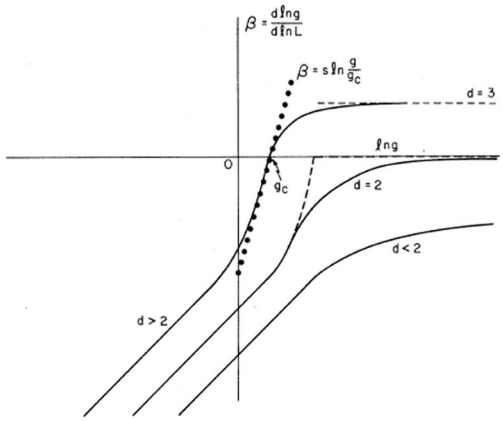

Figure 5.1: β as a function of logarithmic normalized conductance $\ln g$ defined by Eq. (5.1). d denotes the dimension.

β as shown in Fig. 5.1. One of the most important consequences is the following. When we take the macroscopic limit $L \to \infty$, all states are localized and the sample is always insulating in dimensions lower than two, while in more than two dimensions, there is a metal-insulator transition at the critical conductance of g_c, which is an unstable point and any slight deviation drives the electronic system to either a complete insulator or a complete metal in the limit of $L \to \infty$. Therefore, two dimensions are critical separating two extreme states, that is, a metallic state and a insulating state. The above discussion is strictly true for noninteracting electrons.

For a large g, $G(L) = \sigma L^{d-2}$ follows from a usual transport theory, where σ is the conductivity and d is the dimension. We then have $\beta \to d-2$ from Eq. (5.1). Now we consider the perturbation of a weakly disordered case. In three dimensions, because $\beta \to 1$ as $g \to \infty$, we expand β as, within first order, $\beta \cong 1 - c/g$ (c: const.) and we get

$$\sigma_{3\mathrm{D}} \cong \sigma_0 + \frac{c}{L}, \tag{5.2}$$

where σ_0 is given by Eq. (4.1). Similarly, in two dimensions, by putting $\beta \cong -a/g$, we get

$$\sigma_{2\mathrm{D}} \cong \sigma_0 - a \ln\left(\frac{L}{L_0}\right), \tag{5.3}$$

where $\sigma(L_0) = \sigma_0$. Until now, we have considered the case at zero temperature. Because L can be regarded as the length of coherent conduction of an electron, the effects of

temperature and magnetic field are taken into account through L. Magnetic field drives electrons in a cyclotron motion with the maximum radius of $L_H = \sqrt{\hbar/eH}$, which gives $\Delta\sigma_{3\mathrm{D}} \propto H^{1/2}$ and $\Delta\sigma_{2\mathrm{D}} \propto \ln H$ from Eqs. (5.2) and (5.3). On the other hand, raising temperature causes increase in inelastic scattering, which limits the coherent conduction within the inelastic diffusion length $L_{\mathrm{in}} = \sqrt{D\tau_{\mathrm{in}}}$, where D is the diffusion constant and τ_{in} is the inelastic scattering time. When we assume $\tau_{\mathrm{in}} \propto T^{-p}$, we get $\Delta\sigma_{3\mathrm{D}} \propto T^p$ and $\Delta\sigma_{2\mathrm{D}} \propto \ln T$, where p is a constant dependent on the type of the scattering.

The characteristic behaviors of weak localization are the temperature and magnetic field dependencies of the conductivity corrections, that is, $\Delta\sigma(T) = \sigma(T) - \sigma(0)$ and $\Delta\sigma(H) = \sigma(H) - \sigma(0)$. Based on the above discussions, temperature dependence becomes, by recovering $e^2/\hbar$ ($a = c = 1$),

$$\Delta\sigma_{3\mathrm{D}}(T) = \frac{e^2}{\hbar}\sqrt{\frac{\Gamma}{D}}T^{p/2}, \tag{5.4}$$

$$\Delta\sigma_{2\mathrm{D}}(T) = \frac{pe^2}{2\hbar}\log T, \tag{5.5}$$

where Γ is a constant defined by $1/\tau_{\mathrm{in}} = \Gamma T^p$. On the other hand, by formal diagrammatic calculations, magnetic field dependence of the conductivity correction is given by [78]

$$\Delta\sigma_{2\mathrm{D}}(H) = \begin{cases} \dfrac{e^2}{2\pi^2\hbar}\ln\left(\dfrac{4DeH\tau_{\mathrm{in}}}{\hbar}\right), & \left(\dfrac{4D\tau_{\mathrm{in}}eH}{\hbar} \ll 1\right) \quad (5.6\mathrm{a}) \\ \dfrac{e^2}{48\pi^2\hbar}\left(\dfrac{4DeH\tau_{\mathrm{in}}}{\hbar}\right)^2, & \left(\dfrac{4D\tau_{\mathrm{in}}eH}{\hbar} \gg 1\right) \quad (5.6\mathrm{b}) \end{cases}$$

and [79],

$$\Delta\sigma_{3\mathrm{D}}(H) = \begin{cases} \dfrac{0.605e^2}{2\pi^2\hbar}\sqrt{\dfrac{eH}{\hbar}}, & \left(\dfrac{4D\tau_{\mathrm{in}}eH}{\hbar} \ll 1\right) \quad (5.7\mathrm{a}) \\ \sigma_0\left(\dfrac{\tau_{\mathrm{in}}}{\tau}\right)^{3/2}(\omega_c\tau), & \left(\dfrac{4D\tau_{\mathrm{in}}eH}{\hbar} \gg 1\right) \quad (5.7\mathrm{b}) \end{cases}$$

where $\omega_c = eH/m^*$ is the cyclotron frequency and m^* is the orbital effective mass.

5.3 Results and discussions

We estimated sheet carrier density and mobility of $SrTiO_3$ under illumination. Figure 5.2 shows the mobility as a function of the sheet carrier density with different wavelength at 2K. In the figure, connected points are obtained in a series of the measurements. Although there is a large distribution of the data points, we found two types of connected data points. In one type, μ is almost constant as a function of carrier density, while μ is sharply reduced at a certain carrier density in the other type. Although we have not

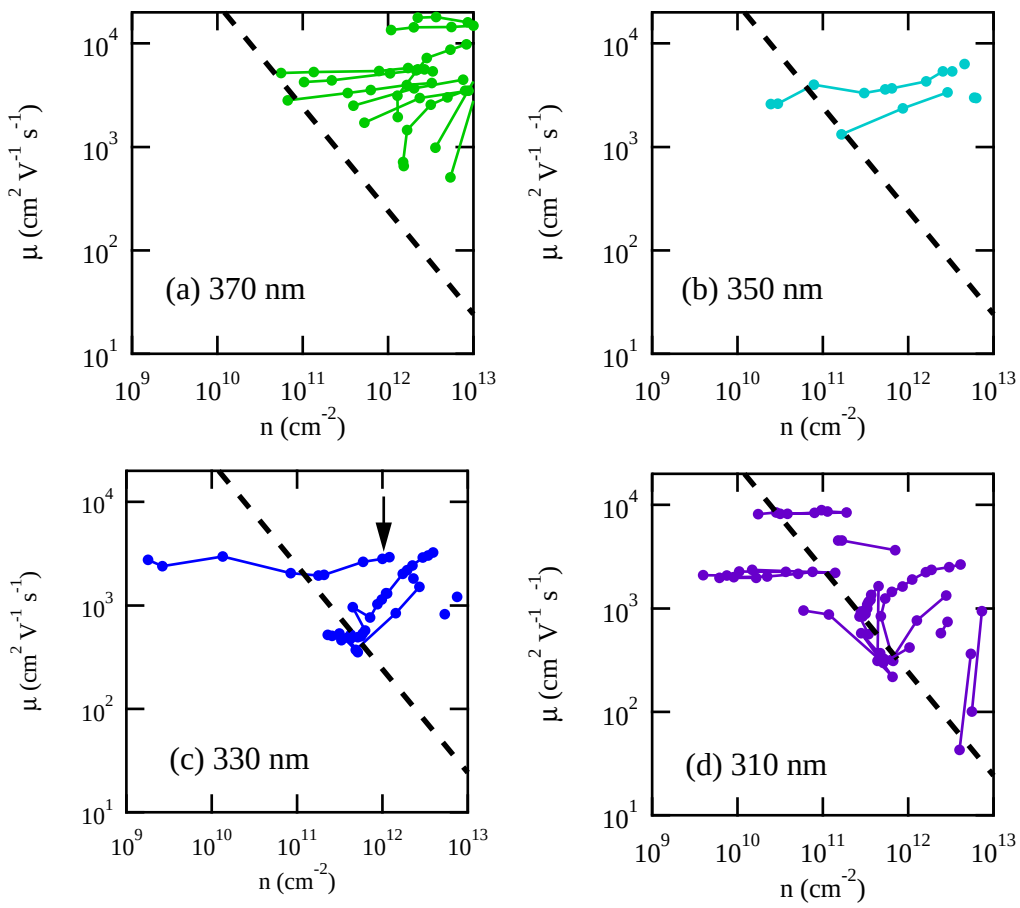

Figure 5.2: Mobility as a function of sheet carrier density with different wavelengths at 2 K. The wavelength of light is (a) 370 nm, (b) 350 nm, (c) 330 nm, and (d) 310 nm. Connected points are obtained in a series of measurement. The broken lines satisfies $e^2/2\pi\hbar = ne\mu$. The arrow in (c) is the sample to be used for measurement of temperature dependence in Fig. 5.3.

understood this discrepancy, this may originate from a detailed historical effect, that is, repetitive uses of a sample or length of time to be irradiated by ultraviolet illumination. Now, we focus on the latter type of state. Almost all such data points are located above the broken lines in Fig. 5.2, which satisfy $\sigma_{\rm min}^{\rm 2D} = e^2/2\pi\hbar = ne\mu$. Here, $\sigma_{\rm min}^{\rm 2D}$ denotes the minimum conductivity in two dimensions. In addition, in some cases, the mobility sharply decreases near the minimum conductivity, particularly under shorter wavelength illumination. On the other hand, under longer wavelength illumination, the reduction of the mobility seems to have no relation with the minimum conductivity. This fact indicates that the electronic conduction is two-dimensional under shorter wavelength illumination, while under the longer wavelength illumination, three-dimensional conduction is suggested.

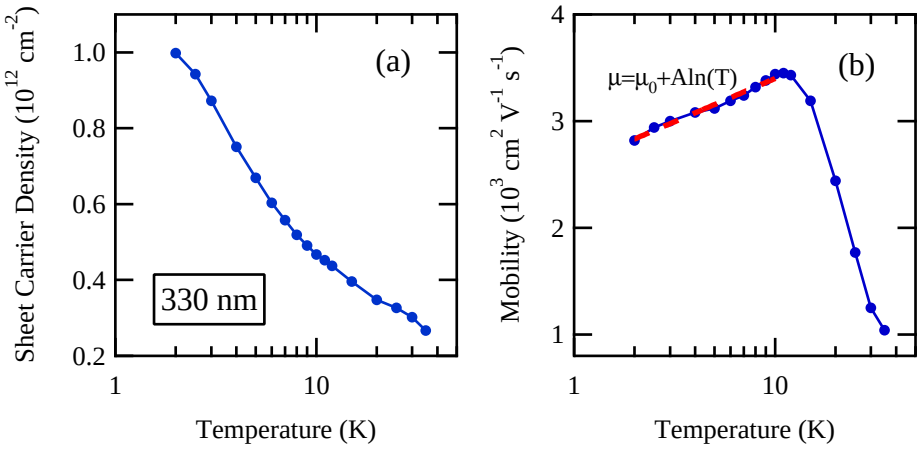

Figure 5.3: Temperature dependence of the (a) carrier density and (b) mobility for a sample indicated by the arrow in Fig. 5.2 under 330 nm illumination. The red broken line in (b) is the result of fitting μ=$\mu_0 + A \ln T$.

We then focused on the case of shorter wavelength illumination. We measured a temperature dependence of carrier density and mobility for a sample indicated by the arrow in Fig. 5.2 (c). Figure 5.3 shows the result under 330 nm illumination, which is compared with Fig. 4.3 in Chapter 4. Because carrier density is not equilibrium and strongly affected by temperature variation, clearly, the mobility continues to decrease as temperature is reduced below 10 K, which means a localizing nature of the carriers. We compare the data with Eq. (5.5) by fitting $\mu = \mu_0 + A\ln(T)$ to the data in Fig. 5.3 (b) from 2 K to 10 K. Since carrier density also varies with temperature, we fixed the carrier density to $n_0 = 10^{11}$ cm^{-2}, for a rough estimation, and we get $A = 350$ cm^2 V^{-1} s^{-1}, which corresponds to $n_0 eA = 5.6 \times 10^{-9}$ Ω^{-1}. This value is much smaller than the theoretically predicted value $e^2/2\hbar = 1.2 \times 10^{-4}$ Ω^{-1} in Eq. 5.5 ($p = 1$). This discrepancy

will be discussed later.

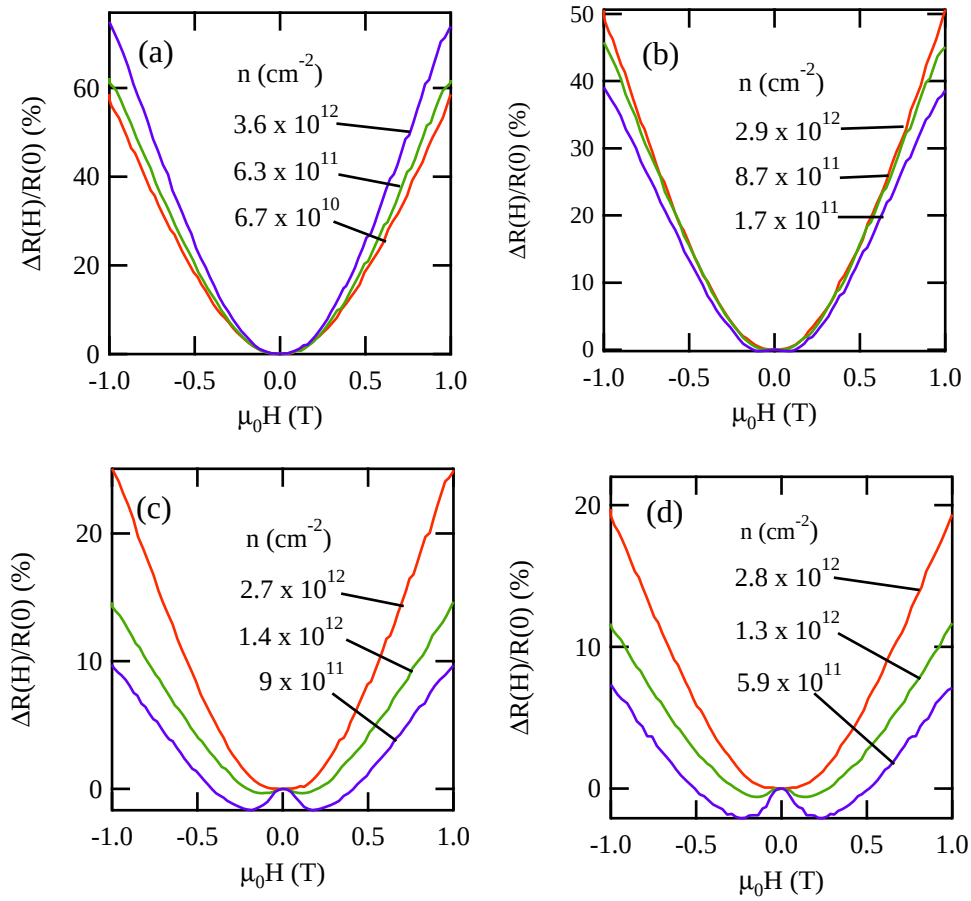

Figure 5.4: MR measurements under (a) 370 nm, (b) 350 nm, (c) 330 nm, and (d) 310 nm with the different light intensities at 2 K.

We also measured the MR because a negative MR should be observed in a weakly localized system. As shown in Fig. 5.4, we did not observed any negative MR under longer wavelength light, while we observed the small negative MR as the carrier density is reduced under shorter wavelength light. This is consistent with the weak localization theory if we take into account the fact that high mobility is observed under longer wavelength light.

In order to confirm the dimensionality, we carried out the MR measurements in three geometries under 310 nm illumination as shown in Fig. 5.5 (a). The result in Fig. 5.5 (b) shows anisotropy, which indicates that this effect originates from a orbital effect and the electronic conduction is two-dimensional because MR in the geometry 1 and geometry 3 could be identical if the conduction were purely three-dimensional. However, even in the geometries 2 and 3, we observed a negative MR. This kind of geometrical dependent MR has been observed in several metallic thin films such as In_2O_3 [80] and attributed to the

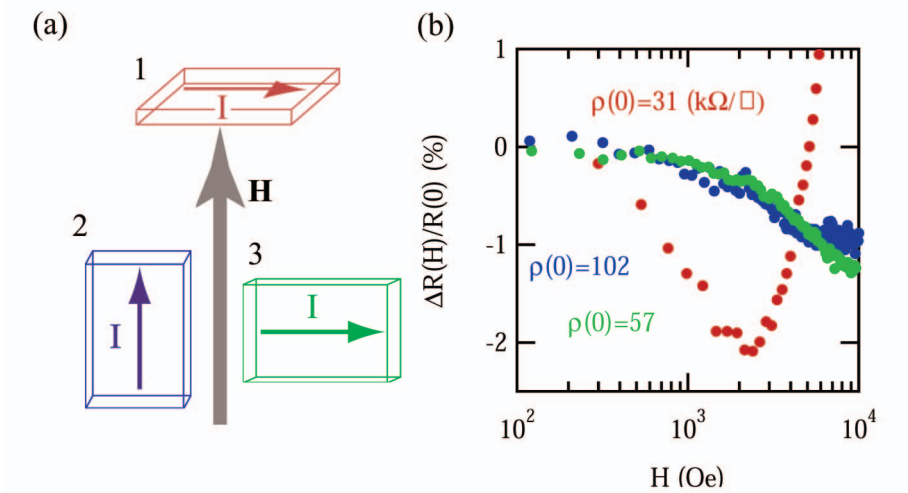

Figure 5.5: (a) Three geometries in MR measurements. 1: $H \perp I$ and $H \perp$ sample surface, 2: $H \parallel I$ and $H \parallel$ sample surface, and 3: $H \perp I$ and $H \parallel$ sample surface. (b) MR measurements at 2 K under 310 nm illumination in the three geometries. Colors correspond to the geometries in (a).

competition between the film thickness and magnetic length $\sqrt{\hbar/eH}$. As H increases, the magnetic length becomes small and eventually crosses the film thickness, where the MR in the geometries 2 and 3 start to be observed. We can then estimate the effective thickness from the MR in such geometries. Figure 5.5 (b) shows that the MR starts to appear at around 0.6 T, which corresponds to 36 nm. If we take into account that the penetration depth of $SrTiO_3$ under 310 nm illumination is about 32 nm as shown in Fig. 5.6 [40], it is relevant to regard the effective thickness as the penetration depth in the case of photocarrier doping. In summary, the above observation can be qualitatively explained as follows. Under 370 nm illumination, the penetration depth is about 10 μm and the conduction is three-dimensional. As the wavelength is reduced, the penetration depth decreases and cross the inelastic diffusion length, which gives rise to two-dimensional conduction. In two dimensions, the effect of localization is evident, compared with the case of three dimensions. This is why we observed the wavelength dependent mobility.

Another difference between shorter and longer wavelengths is the carrier density in three dimensions. In our measurements, typical sheet carrier density 10^{12} cm^{-2} corresponds to about 10^{15} cm^{-3} under 370 nm light, while this sheet carrier density corresponds to 10^{18} cm^{-3} under 310 nm light if we take into account the difference of the penetration depth. In the case of 310 nm light, the Fermi energy is larger than the temperature, while the Fermi energy is smaller than the temperature in the case of 370 nm light, which gives rise to the nondegenerate electron gas. This is another reason we did not observe the weakly localized behavior under 370 nm light even if sheet resistance is around h/e^2 by

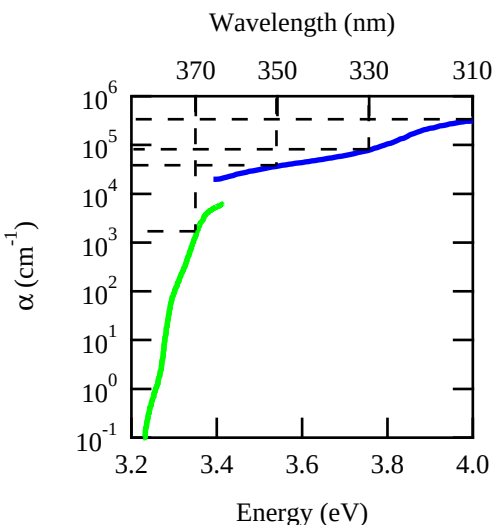

Figure 5.6: Absorption coefficient of $SrTiO_3$ as function of the energy of incident light. From Ref. [40, 41].

reducing the light intensity.

Now we analyze the results quantitatively. The MR in the longitudinal geometry is expressed as [81]

$$\Delta\sigma = \frac{e^2}{\pi\hbar} \ln\left(\frac{tL_{\text{in}}}{\sqrt{12}}\frac{e}{\hbar}H\right), \tag{5.8}$$

where t is the thickness of the film. This is compared with the case of the transverse MR expressed by Eq. (5.6a). Under small magnetic field, the MR is proportional to $\ln H$ and the slope is $e^2/2\pi\hbar$ in the case of transverse MR and $e^2/\pi\hbar$ in the case of longitudinal MR in a linear-log plot. However, our result in Fig. 5.5 shows the MR is about two orders of magnitude smaller than the predicted value in both geometries.

In our case, several conditions are not fulfilled for the observation of weak localization. Because there should be nontrivial distribution of electrons, carriers in each depth contribute to localization effect in a different way. However, in this case, the contributions to the conduction from each layer will be just superposed and does not have a crucial effect. Another condition is that sheet resistance is around h/e^2(=25.8 kΩ) or less in the present case. The weak localization is effective roughly from 1 kΩ to 10 kΩ. In our case, the electronic system is at the crossover point between weak and strong localization, which complicates the analysis. However, in most cases, we do not observe a larger negative MR even though we adjust the resistance optically.

We may need to take into account the nonequilibrium nature of the photocarrier doping. Because we continuously excite carriers, it is not clear whether the Fermi surface is formed in the same way as the case of chemical doping. So far, this point has not been accounted for.

5.4 Conclusion

We mapped out the mobility as a function of the carrier density under illumination with different wavelengths. Although there is a large distribution, the different behavior was clearly observed. Temperature dependence of mobility and MR show that the electronic conduction displays the effect of weak localization under shorter light wavelength, while the effect is absent under longer light wavelength. The difference originates from the different effective thicknesses because of the dependence of the absorption coefficient on the energy of the incident light, which causes different strength of disorder effects and different Fermi energies. By utilizing this property, we can modulate the effective thickness and carrier density just by changing the wavelength and intensity of light.

Chapter 6

High-field Hall measurement of $SrTiO_3$ single crystals

6.1 Introduction

High magnetic field is widely utilized to probe a number of physical quantities in, for example, de Haas-van Alphen effect, cyclotron resonance, electron spin resonance, and nuclear magnetic resonance. The principles are based Landau level splitting of Landau level and Zeeman splitting induced by high magnetic field. It also gives rise to interesting phenomena such as quantum Hall effect [12], which gives precisely quantized Hall resistance unless extended states exists inside the sample because of its topological nature [77].

In this study, we measured Hall resistance up to typically 10 T and found nonlinear magnetic field dependence of the Hall resistance. Although such nonlinear Hall resistance is reminiscent of the anomalous Hall effect (AHE) [84], the peculiar behavior cannot be explained by conventional theories. Although we have not found a satisfactory theory, several unusual conditions are realized in photocarrier-doped $SrTiO_3$, some of which may be relevant to the interpretation of the result.

6.2 Anomalous Hall effect

AHE is a phenomenon in which Hall resistance shows a nonlinear dependence on the applied magnetic field, usually induced by magnetic moments in the sample. E. H. Hall already observed an unusual response of Hall effect in magnetic materials [85] just after the discovery of the Hall effect [86]. In Fig. 6.1, AHE is compared with the ordinary and spin Hall effect [87]. Roughly speaking, AHE takes place in magnetic materials when carriers are deflected to opposite directions dependent on their spins.

In 1954, J. M. Karplus *et al.* demonstrated that a spin-orbit interaction can give rise to the AHE [88]. Just after their suggestion, J. Smit pointed out that the effect of spin-

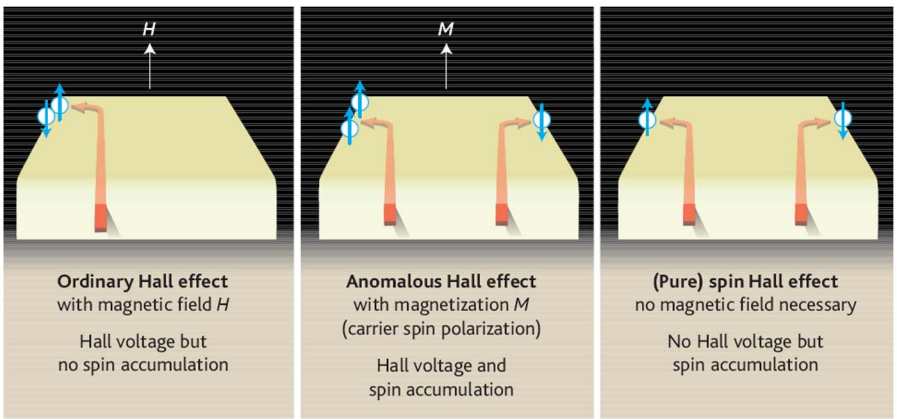

Figure 6.1: (a) Ordinary Hall effect. The carriers are deflected by the magnetic field H to the same direction independent of their spins. (b) Anomalous Hall effect. The carriers are scattered by impurities (extrinsic effect) or deflected by an inherent mechanism of the material (intrinsic effect) to the opposite directions dependent on their spins with magnetization M. (c) Spin Hall Effect. The same situation as (b) except that the material is nonmagnetic. From Ref. [87].

orbit interaction is canceled in a periodic lattice by averaging it out over the unit cell. Instead, they proposed that it originates from spin-dependent scattering with impurities induced by the spin-orbit interaction, which is called skew scattering [89]. Because of unsatisfactory agreement of their model with experiments, L. Berger suggested a side-jump mechanism, which is based on finite displacement in scattering with impurities [90]. These are called extrinsic mechanisms because they are induced by scattering by impurities. Although AHE has been reported in many magnetic materials, almost all results of AHE were interpreted as the superposition of skew scattering and side-jump mechanism, which is

$$\rho_{xy} = R_0 B + 4\pi R_s M, \tag{6.1a}$$

$$R_s \propto \rho_{xx}^n, \tag{6.1b}$$

where ρ_{xy} is the Hall resistivity, R_0 is the normal part of Hall coefficient, B is the magnetic field, R_s is the anomalous part of Hall coefficient, M is the magnetization, and ρ_{xx} is the resistivity. The theories mentioned above predicted $n = 1$ in the skew scattering and $n = 2$ in the side-jump mechanism. In spite of the qualitative agreement with Eq. (6.1), the absolute values are rarely satisfactory, often deviating by orders of magnitude from the estimated values.

Recently, unconventional AHE have been observed in a number of materials with complicated lattice and magnetic structures, which cannot be explained by the conventional theories. Such materials include perovskite manganite [91], pyrochlore molybdate [92],

and spinel compounds [93]. One of the newly proposed theories claimed that a phase in the effective transfer integral gained by the hopping between sites plays an important role in double-exchange ferromagnets [94, 95]. The effective transfer integral in double exchange between i site and j site is expressed as

$$t_{ij} = te^{ia_{ij}} \cos \frac{\theta_{ij}}{2}, \tag{6.2}$$

where t is the transfer integral, a_{ij} is the phase gained by the hopping, and θ_{ij} is the angle of spins between i and j sites. a_{ij} does not affect the hopping probability but affects the interference between electrons, which creates an effective magnetic field $\boldsymbol{b}$ in materials. Since $\boldsymbol{b}$ is proportional to spin chirality, $\boldsymbol{S_i} \cdot \boldsymbol{S_j} \times \boldsymbol{S_k}$ ($\boldsymbol{S_i}$: spin vector in the i site), a noncoplanar spin lattice can produce large effective magnetic field, giving rise to AHE.

Another new theory is based on spin Hall current as shown in Fig. 6.1 (c), where the spin-dependent motion takes place under electric field [96]. The effect is considerable when the spin-orbit interaction is strong and the Fermi energy is located near a band degeneracy. In the case of magnetic material, the imbalance of spins of itinerant electrons produce a charge Hall current, which gives rise to AHE [97]. In contrast to extrinsic AHE, this mechanism is called intrinsic because AHE is induced by inherent band structure.

6.3 Results

Figure 6.2 shows the result of MR and Hall measurements for photocarrier-doped $SrTiO_3$ up to 10 T. The MR is proportional to H^2 in the low magnetic field and tends to saturate as the magnetic field increases, which is explained by the Boltzmann equation [98]. On the other hand, Hall resistance is fairly extraordinary and similar to the AHE [84]. In order to investigate the anomalous behavior, we measured its dependence on carrier density and temperature, and expressed the Hall resistance divided by Hall coefficient obtained from low-field values as a function of magnetic field, as shown in Fig. 6.3. There are several features to be mentioned. First of all, nonlinearity decreases as carrier density increases and temperature increases. Eventually, it almost disappears around 10 K, above which the Hall resistance is almost linear in magnetic field. This fact may indicate that the nonlinearity is not due to extrinsic effects such as undefined sample geometry. Secondly, low-field values seem to give the correct carrier density because of smooth connection of carrier density and mobility as a function of temperature. Otherwise, it could be necessary to assume field dependent carrier density and mobility only below 10 K. Although we have not obtained any satisfactory explanations so far, we discuss the possible origins below.

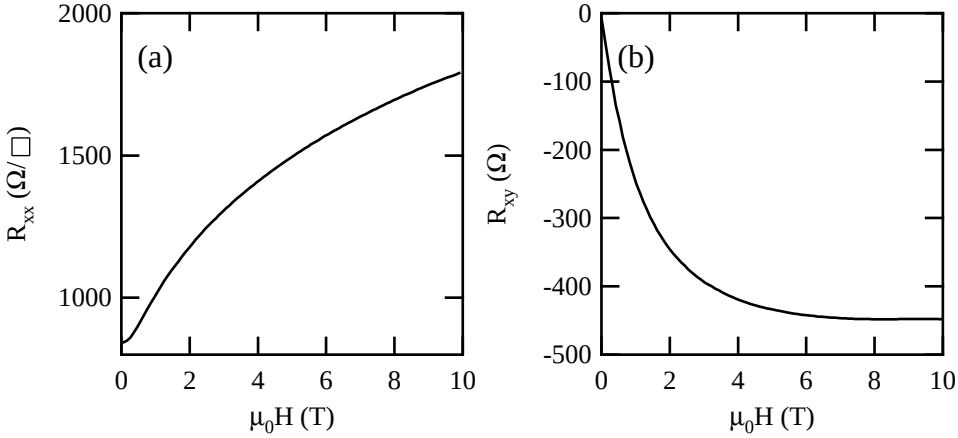

Figure 6.2: (a) MR and (b) Hall measurements at 2 K under 370 nm illumination. The estimated carrier density and mobility are 2.0×10^{12} cm^{-2} and 3700 cm^2 V^{-1} s^{-1}, respectively.

6.4 Discussions

6.4.1 Conventional theories of anomalous Hall effect induced by extrinsic impurities

According to Eq. (6.1), the anomalous part of the Hall effect is proportional to magnetization and the normal part can be estimated above a magnetic field sufficient to saturate magnetization. This does not seem relevant because $SrTiO_3$ is nonmagnetic [99] although we cannot completely rule out the small possibility that residual magnetic impurities have an effect. However, the orientation dependence of MR shown in Fig. 5.5 indicates that spin scattering does not dominate the transport properties in this regime. In addition, as briefly mentioned above, low-field values are experimentally plausible to estimate carrier density against the conventional theories. We conclude that our results cannot be explained by the conventional theories of AHE.

6.4.2 Two-band conduction

When two types of carriers play comparable roles in the conduction, it is possible to observe nonlinear Hall resistance under a certain condition. This can be relevant in the case of semimetals and some semiconductors such as GaAs because the Fermi surface of semimetals consists of electron and hole pockets, while GaAs consists of heavy and light hole pockets. $SrTiO_3$ is another candidate according to experiments explained in Chapter 2 because the Fermi surface consists of heavy and light electron pockets. In addition, both electrons and holes could take part in the conduction when excited by illumination.

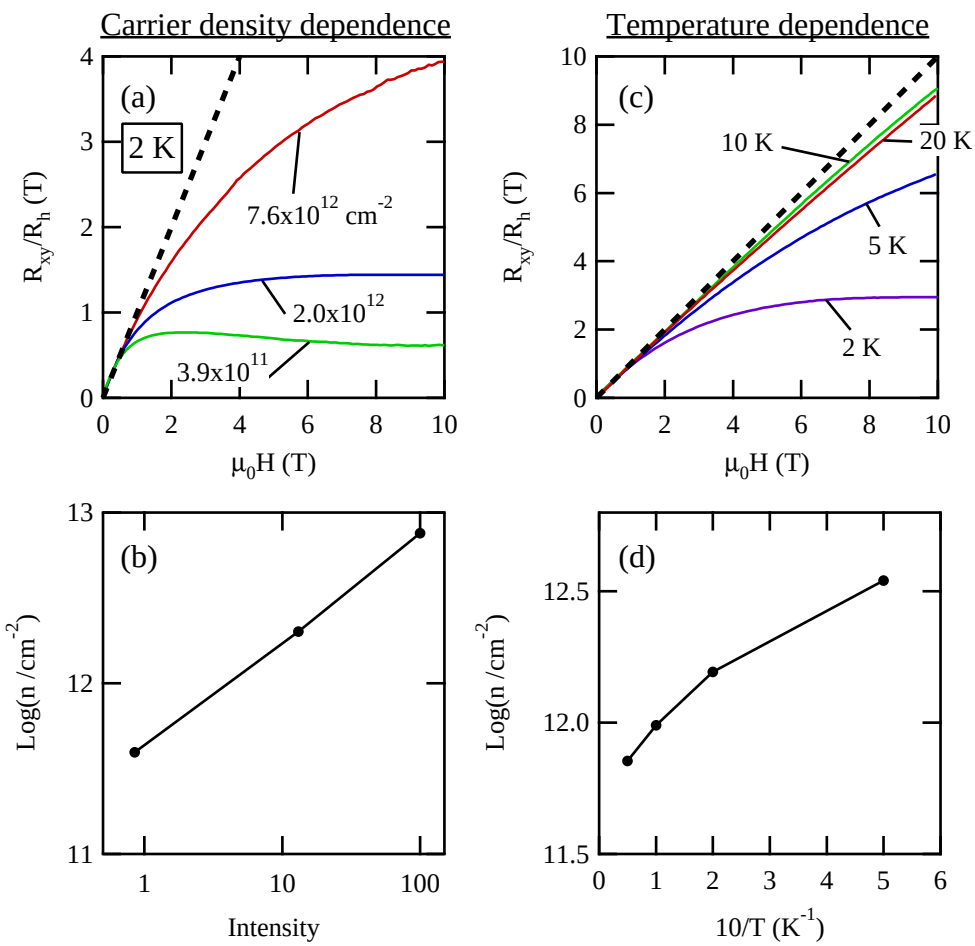

Figure 6.3: Hall resistance divided by Hall coefficient as a function of applied magnetic field with (a) different carrier densities at 2 K and (c) different temperatures. (b) and (d) show the carrier density of corresponding curves in (a) and (c), respectively. Hall coefficient and carrier density were obtained from low-field values. The wavelength of illumination is 370 nm. Mobility ranges from 2000 to 6000 cm^2 V^{-1} s^{-1} depending on temperature and carrier density.

The equation of two-band conduction is expressed as

$$R_H = \frac{(\mu_1^2 n_1 + \mu_2^2 n_2) + (\mu_1 \mu_2 B)^2 (n_1 + n_2)}{e\left[(\mu_1|n_1| + \mu_2|n_2|)^2 + (\mu_1\mu_2 B)^2 (n_1+n_2)^2\right]}, \tag{6.3}$$

where μ_l is the mobility of carriers and n_l (> 0 for holes, < 0 for electrons, l=1 or 2) is the carrier density [100]. In the limiting cases of high and weak magnetic field, these become

$$R_H \to \frac{(\mu_1^2 n_1 + \mu_2^2 n_2)}{e(\mu_1|n_1| + \mu_2|n_2|)^2} \quad (B\mu_{\mathrm{m}} \ll 1), \tag{6.4a}$$

$$R_H \to \frac{1}{e(n_1+n_2)} \quad (B\mu_{\mathrm{M}} \gg 1), \tag{6.4b}$$

where $\mu_{\mathrm{m}} = \min(\mu_1, \mu_2)$ and $\mu_{\mathrm{M}} = \max(\mu_1, \mu_2)$. Only when $B\mu_{\mathrm{m}} < 1 < B\mu_{\mathrm{M}}$, can we observed nonlinear Hall resistance. In our case, it is easy to exclude a possibility that both electrons and holes take part in the conduction because the hole mobility is much smaller than electrons [67], and therefore the contribution of holes is negligible as can be seen in Eq. (6.3). Then we fitted one of the our results by Eq. (6.3) as shown in Fig. 6.4. Because we have four fitting parameters, almost the same fitting curves were

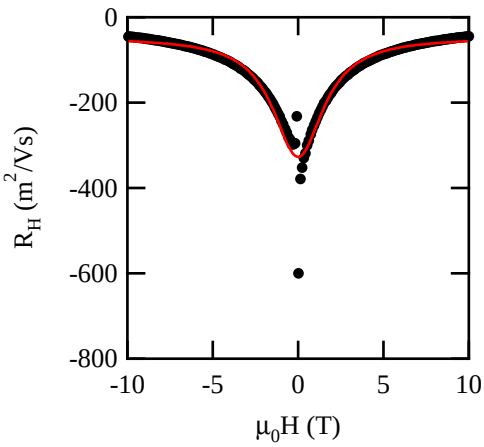

Figure 6.4: Result of fitting to Hall coefficient by Eq. (6.3). Solid circles and the red curve denote data points and fitting curve, respectively. Hall coefficient is calculated by $R_H = R_{xy}/\mu_0 H$ from data in Fig. 6.2. The carrier density and mobility estimated from the low-field value is 2.0×10^{12} cm^{-2} and 3700 cm^2 V^{-1} s^{-1}, respectively.

obtained for various set of parameters. Several set of the fitting parameters are listed in Table 6.1. In spite of the fitting variations, a few features are present. First of all, we need a large difference in mobilities for two types of carriers in order to reproduce nonlinear Hall resistance over such a wide range of magnetic field. In addition, carrier density should be adjusted in order to compensate the difference of mobilities, that is,

n_1 (cm^{-2})	1.2×10^{11}	2.5×10^{11}	9.7×10^{9}
μ_1 (cm^2 V^{-1} s^{-1})	19000	54000	10000
n_2 (cm^{-2})	5.4×10^{11}	5.2×10^{11}	5.5×10^{11}
μ_2 (cm^2 V^{-1} s^{-1})	30	45	9

Table 6.1: Several sets of the fitting parameters to the data in Fig. 6.4. Carriers are electrons and we take absolute values for carrier density in the table.

larger n for smaller μ and vice versa. Secondly, because the effect of temperature can only be included through the change of carrier density or mobility, it is difficult to reproduce the sensitive temperature dependence of the nonlinearity from 2 K to 10 K and lack of dependence above 10 K. This is because mobility is not expected to change significantly below 10 K in analogy with chemically doped cases [8]. Thus we conclude that two-band conduction is extremely unlikely for our results.

6.4.3 Magnetic breakdown

Magnetic breakdown has been observed in metals with large carrier density such as Mg and Au [84]. When a Fermi surface intersects with the first Brillouin zone in momentum space, parts of the Fermi surface are folded with respect to the zone boundary in the reduced zone representation, which forms one electron-like orbit and one hole-like orbit. However, under high magnetic field the orbiting electrons can overcome the gap between the two orbits, and the electron recovers original Fermi surface. This gives rise to magnetic field dependent two-band conduction.

In the case of $SrTiO_3$, although the Fermi surface is small due to small carrier density, magnetic breakdown was observed by the SdH measurement between two electron bands as shown in Fig. 6.5 [31]. Although this could cause nonlinear Hall resistance, it is unlikely in reality because the change of carrier type does not occur in this case and the SdH measurement does not indicate a large difference between mobilities of electrons in the different bands.

6.4.4 Full spin polarization induced by Zeeman splitting

Now we discuss the possibility of large spin polarization because the carrier density of photocarrier-doped $SrTiO_3$ is so small that the Zeeman energy may exceed the Fermi energy. First of all, we estimate the Fermi energy. Sheet carrier density typically ranges from 10^{11} to 10^{13} cm^{-2}. Under the illumination of 370 nm, the penetration depth is about 10 μm from a absorption measurement [41]. As an approximation, we neglect the distribution and diffusion of carriers along the depth and just assume that carriers are

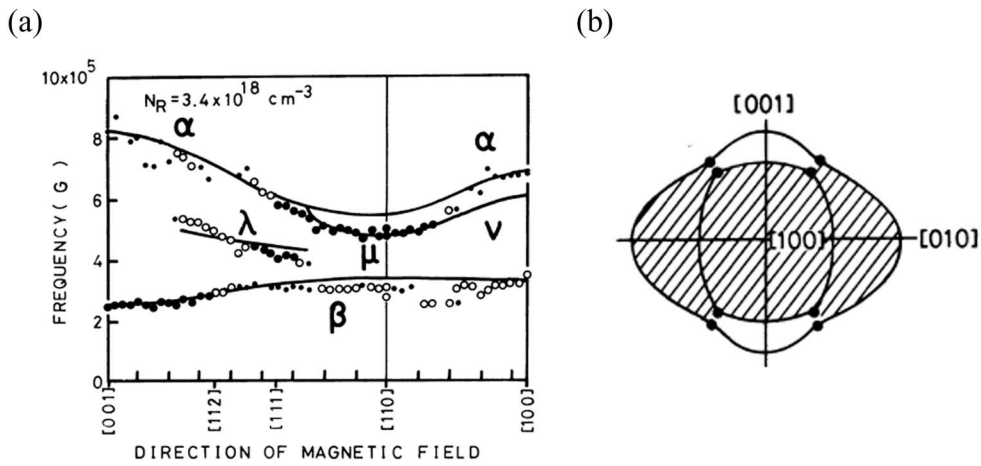

Figure 6.5: (a) Observed SdH frequency as a function of direction of magnetic field. λ, μ, and ν branches correspond to Fermi surfaces with magnetic breakdown. (b) One of the estimated Fermi surface along [100] direction. Shaded area corresponds to ν branch. From Ref. [31].

uniformly distributed within the depth of 10 μm, which gives the carrier density in three dimensions from 10^{14} to 10^{16} cm^{-3}. Then, using the Fermi energy and carrier density reported from SdH measurement ($E_F = 4.2$ meV when $n = 3.4 \times 10^{18}$ cm^{-3}) [31], we estimate the Fermi energy within the free carrier approximation, $E_F \propto n^{2/3}$, and we get E_F from 4.0×10^{-3} to 8.6×10^{-2} meV. Because 1 K corresponds to 8.6×10^{-2} meV, Fermi energy is less than the measurement temperature and, moreover, less than the Zeeman splitting, $g\mu_B H$ (μ_B: Bohr magnetron), under 1 T with g factor of 2 [101], which corresponds to 1.2×10^{-1} meV. This estimation suggests full spin polarization under strong magnetic field when the energy of temperature is less than Zeeman splitting. If Zeeman splitting plays an important role in our result of nonlinear Hall resistance, the data in Fig, 6.3 (c) must scale with temperature. Figure 6.6 shows the result renormalized by temperature. The correspondence of curves with different temperatures is not so satisfactory. However, because the difference is not too big, inclusion of simplified factors such as carrier density profile should be taken into account. However, even though Zeeman splitting gives rise to full spin polarization, we cannot explain our results by the conventional theories.

6.4.5 Intrinsic anomalous Hall effect

In this case, Fermi energy must be near a band degeneracy. As mentioned in the Chapter 2, two of the t_{2g} bands of $SrTiO_3$ is degenerate at $\boldsymbol{k} = 0$ and the degeneracy is lifted by the spin-orbit interaction. This is the exactly the same case as the valence band of GaAs, as discussed in Ref. [96]. We then need a imbalance of spin density, which can

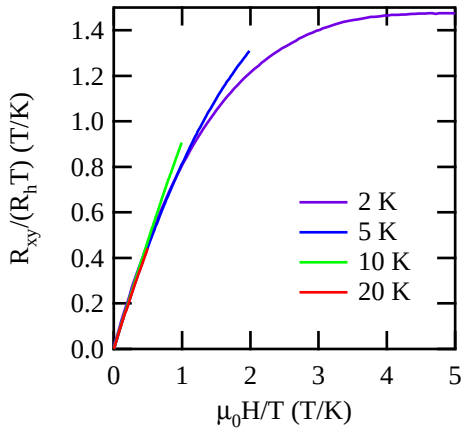

Figure 6.6: Hall resistance as a function of magnetic field renormalized by temperature.

actually be caused by Zeeman splitting as discussed above. Although we need a strict calculation of the gauge field for the complete analysis, we will just give some simple estimations below.

In the case of $SrTiO_3$, because the energy of the spin-orbit interaction was estimated to be 1.54 meV [43], this effect holds up to about 20 K. In this sense, our result is not compatible with the theory of intrinsic AHE because the anomalous term almost disappears above 10 K as shown in Fig. 6.3 (b). However, Zeeman splitting is also affected by temperature, which determines magnetic field where the Hall resistance starts to deviate. This shift of the characteristic magnetic field is present in Fig. 6.3 (b) and this magnetic field is almost fixed at the constant temperature with different carrier density as shown in Fig. 6.3 (a), which means that Zeeman splitting is obscured by temperature under small magnetic field. In magnetic materials, however, AHE almost saturates above the magnetic field of the saturation of magnetization. 1 T is enough for the magnetization to saturate in our case. Therefore, we need a mechanism to cause the nonlinearity above the saturation magnetic field. It has been shown that, in the case of intrinsic AHE, the behavior is rather sensitive to the chemical potential [102]. In our case, a chemical potential shift is actually caused by magnetic field because the zero point energy of Landau level $\hbar\omega_c/2$, can be larger than Fermi energy. This chemical potential shift may give rise to our AHE.

We then discuss carrier density dependence in Fig. 6.3 (a). The gauge field is a delta function at $\boldsymbol{k} = 0$ in the clean limit of $\tau \to \infty$, while it is broadened by impurity scattering, causing finite τ, where τ is the relaxation time of an electron. As carrier density increases, the ratio of carriers near $\boldsymbol{k} = 0$ decreases, which causes the insensitivity to the gauge field.

Now, we discuss the effect of relaxation time. The broadening of energy is given by $\Delta E = \hbar/\tau$. In our case, typical value of mobility $\mu = 5000$ cm^2 V^{-1} s^{-1} gives $\tau = 4.0 \times 10^{-11}$ s ($m^* = 1.4m_0$ [31], m_0: mass of an free electron) and $\Delta E = 0.17$ meV, which is comparable to temperature of 1.9 K. Then this broadening does not affect the above discussion. Figure 6.7 compares the case of low mobility with the case of high mobility. The low mobility sample was obtained by long ultraviolet irradiation. It is clear that the anomalous term is strongly damped even under similar conditions because $\mu = 500$ cm^2 V^{-1} s^{-1} corresponds to 19 K. However, compared with the case of 20 K in real temperature in Fig. 6.3, the AHE term is still present. For the relevance of this theory to our results, numerical calculation should be performed.

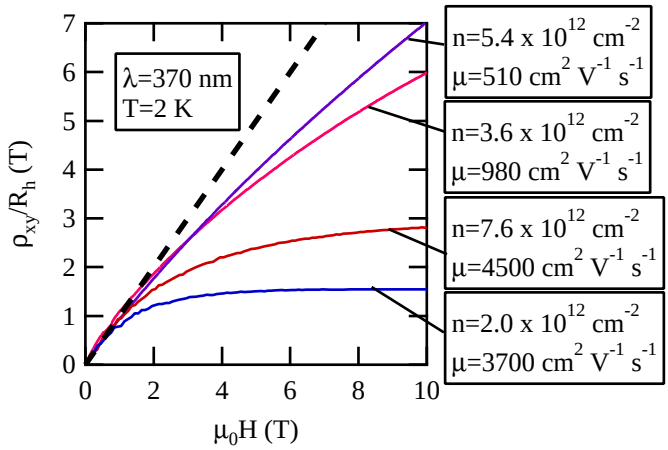

Figure 6.7: Hall resistance divided by Hall coefficient from low-field values under 370 nm illumination at 2 K with different carrier densities (n) and mobilities (μ).

6.5 Conclusions

In this study, we observed unconventional AHE. Although we phenomenologically conclude that the low-field value gives the correct Hall coefficient, the behavior cannot be explained by conventional theories of AHE as well as other existing theories which gives rise to nonlinear Hall resistance. We also considered the results based on a theory recently proposed in connection with the spin Hall effect. Although it is difficult to specify the origin due to the absence of numerical calculations, several estimates seem to be compatible with the new theory. In our speculation, given the band dispersion of $SrTiO_3$ including spin-orbit interaction, we need unusually small Fermi energy for the observation of the nonlinearity. In addition, Zeeman splitting and the Landau level structure should be taken into account. Moreover, in order to reduce the broadening

of energy, low temperature and long relaxation time are necessary. For such complex mechanism, numerical analysis will clarify the validity.

Chapter 7

Photoconductivity of $SrTiO_3$ thin films

7.1 Introduction

Because of the availability of high quality substrates [103], $SrTiO_3$ has been regarded as a prototypical material to investigate the kinetics of thin film growth [104–106]. Given established technique to grow high quality films [107], a variety of applications are feasible, for example, as a gate dielectrics [109] and a channel layer [15, 108] in a field-effect transistor. So far, however, only single crystals have been used in the studies on photoconductivity of $SrTiO_3$. Photogenerated carriers in single crystal substrates were also utilized in recent studies on photocarrier injection to oxide thin films [19]. Then it is quite valuable to investigate the photoconductivity of $SrTiO_3$ thin films. The establishment of these phenomena in films will give much a wider range of options to utilize photoinduced phenomena in oxide heterointerfaces.

In this study, we deposited $SrTiO_3$ thin films by PLD and investigated the photoconductivity. We used nonsteped LSAT ($[LaAlO_3]_{0.3}[SrAl_{0.5}Ta_{0.5}O_3]_{0.7}$) as substrates in the first step because of the large substrate band gap ($E_g = 4.7$ eV [110]) and the small lattice mismatch with $SrTiO_3$ ($a_{\mathrm{LSAT}} = 3.87$ Å in pseudocubic perovskite [111]). As a result, we observed that some of the films showed photoconductivity but with degraded mobility and low efficiency of carrier generation. We will discuss the origins.

7.2 Experimental

In advance of the deposition, the LSAT substrate was ultrasonically washed in acetone and methanol and fixed by clamps on a nickel plate with platinum paste. Subsequently, the substrate was set in the vacuum chamber and heated at the same temperature as for deposition for 30 minutes. During deposition, the oxygen partial pressure was kept at 1×10^{-6} Torr and temperature was changed as parameters of growth. After the

deposition, temperature was cooled down to 400 °C and oxygen pressure was increased to about 760 Torr in order to fill oxygen vacancy by postannealing. The quality of sample was characterized by AFM and XRD. Photoconductivity was measured using a PPMS and a ultraviolet Xe lamp.

7.3 Results

Figure 7.1 (a) and (b) show typical RHEED patterns before and after the deposition, respectively, which indicates that the well defined surface of substrate and two-dimensional growth on it. The RHEED oscillation was not observed probably due to step-flow growth above 1000 °C as shown in Fig. 7.1 (c). Figure 7.2 shows the results of AFM and RSM

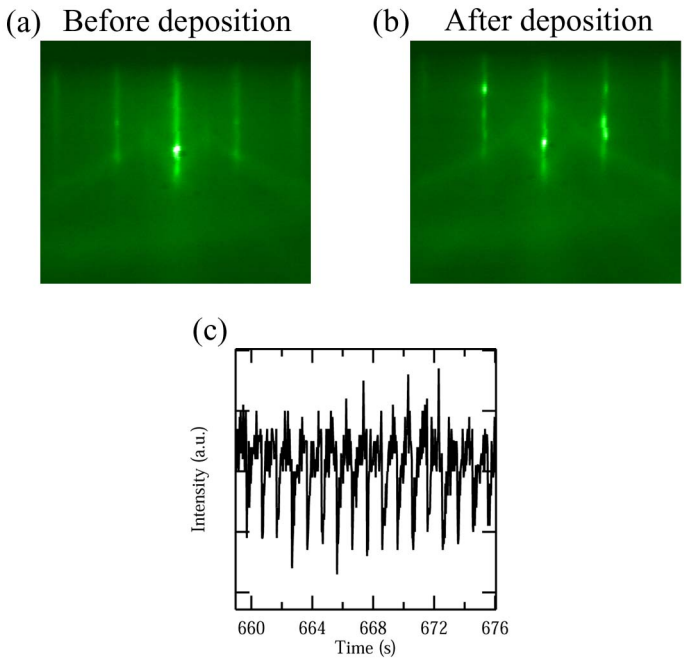

Figure 7.1: RHEED patterns (a) before deposition and (b) after deposition. (c) RHEED intensity during growth. The growth conditions are 1100 °C and 1×10^{-6} Torr.

measurements on thin films grown at different temperatures. As we can see, as the temperature increases, the surface becomes smoother and the step-and-terrace structure gradually appears. This is because the high temperature annealing before deposition reconstruct a stepped substrate surface and the adatoms becomes more energetic, giving rise to a step-flow growth. The RSM shows the relaxation of the lattice to the value of the bulk, 3.905 Å, as the growth temperature increases as indicated in Fig. 7.3. This tendency is common in thin film growth [63].

We then characterized the photoconductivity of thin films. We found that only about

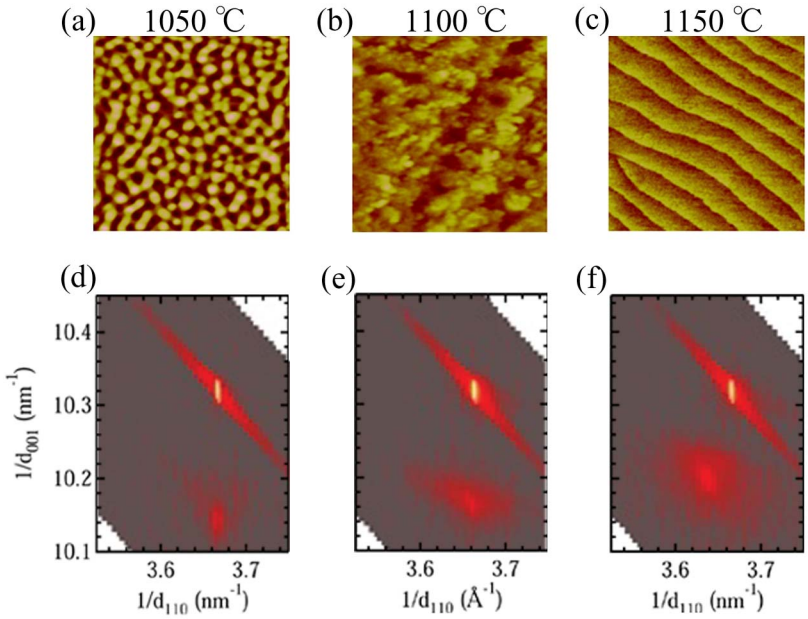

Figure 7.2: AFM images of the thin films grown at (a) 1050 °C, (b) 1100 °C, and (c) 1150 °C and (d) (e) (f) corresponding RSM, respectively. The scales of height are 5 nm in (a) and (b) and 2 nm in (c).

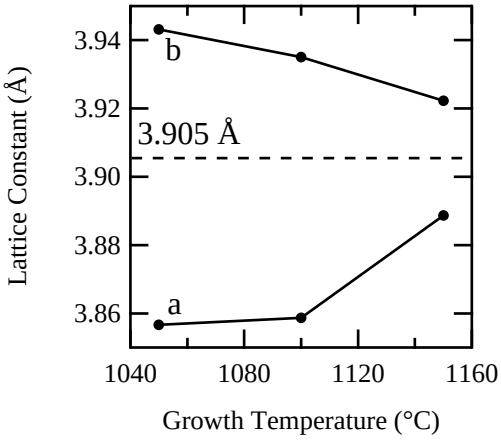

Figure 7.3: In-plane (a) and out-of-plane (b) lattice constants obtained from RSM in Fig. 7.2 as a function of growth temperature.

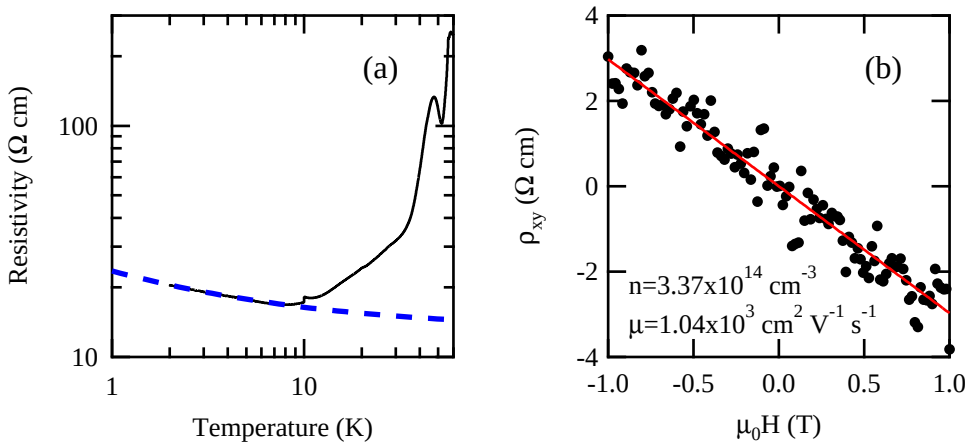

Figure 7.4: (a) Resistivity of a $SrTiO_3$ thin film as a function of temperature under 350 nm illumination. The blue broken line is the result of fitting by $\rho = \rho_0 + AT^{-1/2}$, where $\rho_0 = 13\ \Omega^{-1}\ \mathrm{cm}^{-1}$ and $A = 10\ \Omega^{-1}\ \mathrm{cm}^{-1}\ \mathrm{K}^{1/2}$. (b) Hall measurement at 10 K. The carrier density and mobility were estimated by linear fitting as shown by red line in (b). The growth conditions are 1100 °C and 1×10^{-6} Torr. The film thickness is 1375 Å.

half of the samples showed photoconductivity within a measurable range, which is typically up to about 1 GΩ. For such samples, we confirmed that photoconductivity is considerably reduced under 370 nm illumination, compared with shorter wavelength. Taking into account that photoconductivity is the largest under 370 nm illumination in the case of $SrTiO_3$ single crystals, this is consistent with the fact that the penetration depth around this wavelength is between the thickness of substrate and film thickness. Figure 7.4 shows the result of photoconductivity measurement of a film grown at 1100 °C with the thickness of 1375 Å. Temperature dependence of resistivity is almost metallic although nonmonotonic features were observed at intermediate temperature. In analogy with the case of single crystal, the behavior may originate from the change of mobility at low temperature and the change of carrier density in higher temperature particularly above 35 K, where resistance sharply starts to increase. At low temperature, the resistance increases as $T^{-1/2}$. This is reminiscent of electron interaction effects and the expression is given by [82]

$$\sigma_{3\mathrm{D}}(T) = \sigma_0 \left[1 + \frac{\alpha}{k_F l} \left(\frac{kT\tau}{\hbar} \right)^{1/2} \right], \tag{7.1}$$

where α is a constant, k_F is the Fermi wavenumber, and l is the mean free path. However, this equation is only valid in the metallic regime $k_F l \gg 1$ and we do not discuss the result here. We then carried out Hall measurement, which we found linear as a function of magnetic field at least up to 5 T as shown in Fig. 7.4 (b). Assuming that carriers are extended uniformly in the film, at 10 K, the carrier density is estimated to be about

3×10^{14} cm^{-3}, which corresponds to the sheet carrier density of 3×10^{9} cm^{-2}. This value is almost four orders of magnitude less than the case of single crystal $SrTiO_3$. On the other hand, the mobility was 1×10^{3} cm^{2} V^{-1} s^{-1}, which is about one order smaller. The origin of the degradation will be discussed later.

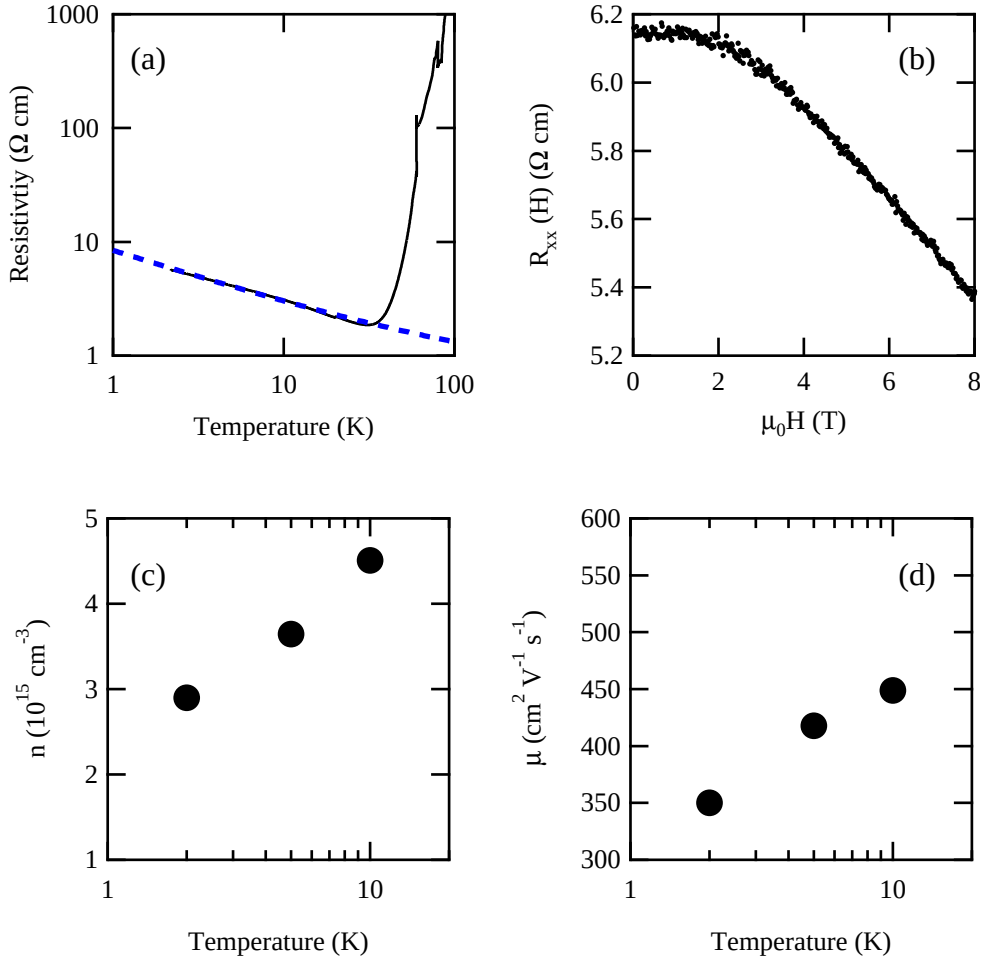

Figure 7.5: (a) Resistivity of a $SrTiO_3$ thin film as a function of temperature under 360 nm illumination. The blue broken line is the result of fitting by $\rho = \rho_0 + AT^{-1/2}$, where $\rho_0 = 0.53\ \Omega^{-1}$ cm^{-1} and $A = 7.9\ \Omega^{-1}$ cm^{-1} K$^{1/2}$. (b) Transverse magnetoresistance at 2 K. (c) Carrier density and (d) mobility as a function of temperature. This film was deposited under the same growth conditions as the sample in Fig. 7.5. The film thickness is 1860 Å.

Figure 7.5 shows the results from a different sample from the film in Fig. 7.4 but grown under the same conditions. As shown in Fig. 7.5 (a), although temperature dependence photoconductivity is qualitatively similar, the absolute values are rather different, compared with the data in Fig. 7.4 (a). In addition, carrier density was about twice, while the mobility is about half, which did not show strong temperature dependence below 10 K as shown in 7.5 (c) and (d). Figure 7.5 (b) shows the transverse MR at 2 K. We found

that the MR was negative up to 8 T and this is common in almost all thin film samples which show photoconductivity. Although negative MR was predicted by the theory of electron correlation effects with disorder, this behavior cannot be explained because MR is predicted to be proportional to H^2 in weak magnetic field and $H^{1/2}$ in strong magnetic field [83]. We have not understood the origin so far.

7.4 Discussions

We found the degraded efficiency of carrier generation and mobility in $SrTiO_3$ thin films. In the case of thin films, similar degradations have been observed in dielectric constant [112] and carrier activation and mobility in Nb-doped $SrTiO_3$ [113] compared with the single crystal [8, 10]. This was attributed to a intrinsic effect which originates from a soft-mode hardening [114]. In some cases, these are attributed to the strain from substrates [115], causing a high density of dislocations [116]. This may be relevant in our case due to the -0.9 % lattice mismatch between $SrTiO_3$ and LSAT, although this value is small. Another possible factors may be the growth conditions such as low growth temperature or high oxygen partial pressure, which also causes poor crystallinity. In order to improve it, high temperature and low pressure have been utilized [107]. Recently, it has been suggested that laser conditions can strongly affect the ratio between Sr and Ti cations in films deposited by PLD [105]. In Fig. 7.6, we compared our study with the

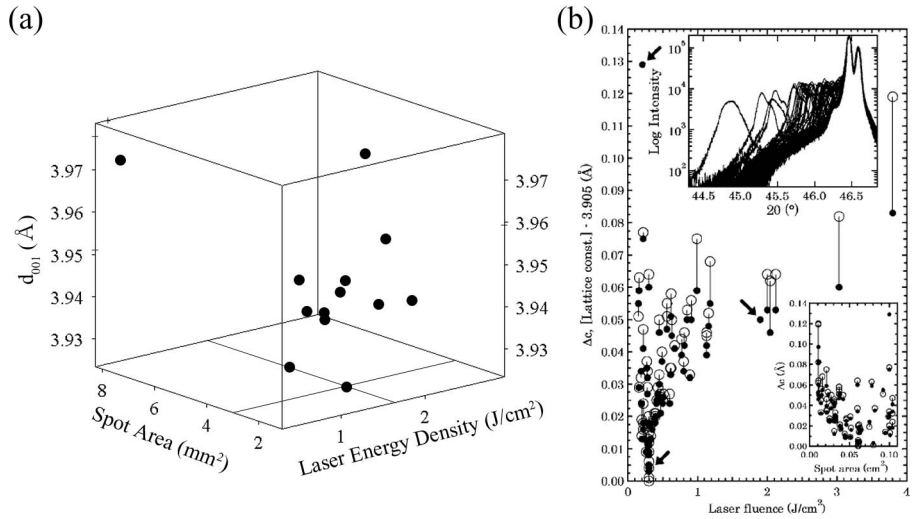

Figure 7.6: (a) Out-of-plane lattice parameter of $SrTiO_3$ films grown on LSAT substrates as functions of laser energy and spot area. Growth temperature and oxygen partial pressure were 750 °C and 1×10^{-6} Torr, respectively. (b) The same study using $SrTiO_3$ substrates from Ref. [105]. Growth temperature and oxygen partial pressure were 700 °C and 1×10^{-6} Torr, respectively. The thickness is 1000 Å for all samples in (a) and (b).

result from Ref. [105] on the out-of-plane lattice parameter as functions of laser energy and spot area. In spite of a small number of data points in our results, a similar tendency was observed to the result in the reference. In our case, the optimal laser conditions are the laser energy density of 1.6 J/cm^2 and spot area of 3 mm^2, respectively, within existing data points, which gives out-of-plane lattice constant of 3.924 Å. Although more data points are necessary to compare our data with Ref. [105], the optimal conditions obtained above can be regarded as more or less optimal if we take into account the difference of substrates.

7.5 Conclusions

In this study, we studied the photoconducting properties of $SrTiO_3$ thin films grown on LSAT substrates. We found that the efficiency of carrier generation and mobility were degraded to some extent, compared with the case of single crystal. There are several factors to be considered such as lattice strain and laser conditions. In our speculation, lattice strain could be removed by using a buffer layer followed by high-temperature annealing [117]. In addition, if stoichiometry plays an important role as in Ref. [105], the optimization makes it possible to control the photoconducting state by laser conditions. These are left to future investigations.

Chapter 8

Conclusions

Although optical control of physical properties has been widely utilized for semiconductors, this is still an infant area for TMOs. In such materials, incident photons do not just create electron-hole pairs but affect the whole system through their inherent strong correlations. Nonequilibrium nature of the photoexcitation can even open hidden quasi-stable states [118]. Among TMOs, $SrTiO_3$ can be regarded as a representative material because of its complex photoresponse.

In this thesis, we studied the photoconducting state of $SrTiO_3$ from a variety of aspects. In spite of the long history of $SrTiO_3$, we observed several new phenomena. One of the aspects of our work is to characterize the photoconducting state at low temperature under high magnetic field. We found that, in contrast to chemically doped $SrTiO_3$, the magnetotransport properties contained many unknown phenomena such as the nonlinear Hall resistance as a function of magnetic field. We also utilized the advantages of the photocarrier doping, which enabled us to study the electronic transport properties in the vicinity of the metal-insulator transition because of the uniform doping and the precise tuning of the carrier density. We found the weakly localized properties in a range of low carrier density, which cannot be achieved by the present technique of chemical doping for $SrTiO_3$. Although such phenomena were observed independent of samples, we found different carrier generation efficiency in a sample dependent manner at intermediate temperature between 30 K and 100 K. The difference is quite similar to the discrepancies among previous reports on photocarrier-doped $SrTiO_3$. So far, we have not understood which photoconducting property is intrinsic. Investigations into the microscopic origins should be performed.

Since $SrTiO_3$ shows the complex physical properties as discussed in Chapter 2, correlations between the photoexcited carriers and other such properties are interesting issues. In particular, superconductivity of the photogenerated carriers is a fairly attractive subject to investigate in the future because a modification of the phonon structure by ultraviolet illumination was suggested [119], which could affect its superconducting

state.

Much attention to optical control of oxide heterointerfaces has been drawn by the recent impressive studies on photocarrier injection to oxide thin films grown on $SrTiO_3$ substrates [19]. Although photocarrier generation of $SrTiO_3$ thin films we deposited is not as efficient as bulk $SrTiO_3$, the availability of the high-quality thin films will enable us to fabricate a new type of heterojunctions controlled by photons. Because oxide heterojunctions have been intensively studied in recent years, optical control of such heterointerfaces will be a growing field. Our studies can play an important role as a basis in the field.

Bibliography

[1] H. Shirakawa, E. J. Louis, A. G. MacDiarmid, C. K. Chiang, and A. J. Heeger, Synthesis of Electrically Conducting Organic Polymers: Halogen Derivatives of Polyacetylene, $(CH)_x$, J. Chem. Soc., Chem. Commun. **16**, 578 (1977).

[2] G. E. Moore, Cramming More Components onto Integrated Circuits, Electronics **38**, 114 (1965).

[3] S. M. Sze, *Physics of Semiconductor Devices*, 2nd ed. (John Wiley & Sons, Inc., New York, 1981).

[4] J. G. Bednorz and K. A. Müller, Possible High T_c Superconductivity in the Ba-La-Cu-O System, Z. Phys. B **64**, 189 (1986).

[5] A. P. Malozemoff, J. Mannhart, and D. Scalapino, High-Temperature Cuprate Superconductors Get to Work, Physics Today **58**, 41 (2005).

[6] Y. Tokura and N. Nagaosa, Orbital Physics in Transition-Metal Oxides, Science **288**, 462 (2000).

[7] C. H. Ahn, J.-M. Triscone, and J. Mannhart, Electric Field Effect in Correlated Oxide Systems, Nature (London) **424**, 1015 (2003).

[8] Electron Mobility in Semiconducting Strontium Titanate, O. N. Tufte and P. W. Chapman, Phys. Rev. **155**, 796 (1967).

[9] R. Willett, J. P. Eisenstein, H. L. Störmer, D. C. Tsui, A. C. Gossard, and J. H. English, Observation of an Even-Denominator Quantum Number in the Fractional Quantum Hall Effect, Phys. Rev. Lett. **59**, 1776 (1987).

[10] K. A. Müller and H. Burkard, $SrTiO_3$: An Intrinsic Quantum Paraelectric Below 4 K, Phys. Rev. B **19**, 3593 (1979).

[11] J. F. Schooley, W. R. Hosler, and M. L. Cohen, Superconductivity in Semiconducting $SrTiO_3$, Phys. Rev. Lett. **12**, 474 (1964).

[12] K. v. Klitzing, G. Dorda, and M. Pepper, New Method for High-Accuracy Determination of the Fine-Structure Constant Based on Quantized Hall Resistance, Phys. Rev. Lett. **45**, 494 (1980).

[13] D. C. Tsui, and A. C. Gossard, Resistance Standard Using Quantization of the Hall Resistance of GaAs-$Al_xGa_{1-x}As$ Heterostructures, Appl. Phys. Lett. **38**, 550 (1981).

[14] K. Shibuya, T. Ohnishi, T. Uozumi, T. Sato, M. Lippmaa, M. Kawasaki, K. Nakajima, T. Chikyow, and H. Koinuma, Field-Effect Modulation of the Transport Properties of Nondoped $SrTiO_3$, Appl. Phys. Lett. **88**, 212116 (2006).

[15] H. Nakamura, H. Takagi, I. H. Inoue, Y. Takahashi, T. Hasegawa, and Y. Tokura, Low Temperature Metallic State Induced by Electrostatic Carrier Doping of $SrTiO_3$, Appl. Phys. Lett. **89**, 133504 (2006).

[16] H. P. Wei, D. C. Tsui, and M. Razeghi, Persistent Photoconductivity and the Quantized Hall Effect in $In_{0.53}Ga_{0.47}As$/InP Heterostructures, Appl. Phys. Lett. **45**, 666 (1984).

[17] N. Bichel, G. Schmidt, K. Heinz, and K. Müller, Ferroelectric Relaxation of the $SrTiO_3$(100) Surface, Phys. Rev. Lett. **62**, 2009 (1989).

[18] M. Stengel and N. A. Spaldin, Origin of the Dielectric Dead Layer in Nanoscale Capacitors, Nature (London) **443**, 679 (2006).

[19] Y. Muraoka and Z. Hiroi, Photocarrier Injection to Transition Metal Oxides, J. Phys. Soc. Jpn. **72**, 781 (2003).

[20] A. Ohtomo and H. Y. Hwang, A High-Mobility Electron Gas at the $LaAlO_3/SrTiO_3$ Heterointerface, Nature (London) **427**, 423 (2004).

[21] T. Feng, Anomalous Photoelectronic Processes in $SrTiO_3$, Phys. Rev. B **25**, 627 (1982).

[22] J. A. Noland, Optical Absorption of Single-Crystal Strontium Titanate, Phys. Rev. **94**, 724 (1954).

[23] H. P. R. Frederikse and W. R. Hosler, Hall Mobility in $SrTiO_3$, Phys. Rev. **161**, 822 (1967).

[24] C. Lee, J. Yahia, and J. L. Brebner, Electronic Conduction in Slightly Reduced Strontium Titanate at Low Temperatures, Phys. Rev. B **3**, 2525 (1971).

[25] C. S. Koonce, M. L. Cohen, J. F. Schooley, W. R. Hosler, and E. R. Preiffer, Superconducting Transition Temperatures of Semiconducting $SrTiO_3$, Phys. Rev. **163**, 380 (1967).

[26] H. Suzuki, H. Bando, Y. Ootuka, I. H. Inoue, T. Yamamoto, K. Takahashi, and Y. Nishihara, Superconductivity in Single-Crystalline $Sr_{1-x}La_xTiO_3$, J. Phys. Soc. Jpn. **65**, 1529 (1996).

[27] H. Unoki and T. Sakudo, Electron Spin Resonance of Fe^{3+} in $SrTiO_3$ with Special Reference to the 110°K Phase Transition, J. Phys. Soc. Jpn. **23**, 546 (1967).

[28] T. Sakudo and H. Unoki, Dielectric Properties of $SrTiO_3$ at Low Temperatures, Phys. Rev. Lett. **26**, 851 (1971).

[29] H. P. R. Frederikse, W. R. Hosler, W. R. Thurber, J. Babiskin, and P. G. Siebenmann, Shubnikov–de Haas Effect in $SrTiO_3$, Phys. Rev. **158**, 775 (1967).

[30] B. Gregory, J. Arthur, and G. Seidel, Measurements of the Fermi Surface of $SrTiO_3$:Nb, Phys. Rev. B **19**, 1039 (1979).

[31] H. Uwe, R. Yoshizaki, T. Sakudo, A. Izumi, and T. Uzumaki, Conduction Band Structure of $SrTiO_3$, Jpn. J. Appl. Phys. **Suppl.24-2**, 335 (1985).

[32] A. H. Kahn and A. J. Leyendecker, Electronic Energy Bands in Strontium Titanate, Phys. Rev. **135**, A1321 (1964).

[33] L. F. Mattheiss, Energy Bands for $KNiF_3$, $SrTiO_3$, $KMoO_3$, and $KTaO_3$, Phys. Rev. B **6**, 4718 (1972).

[34] L. F. Mattheiss, Effect of the 110°K Phase Transition on the $SrTiO_3$ Conduction Bands, Phys. Rev. B **6**, 4740 (1972).

[35] H. P. R. Frederikse, W. R. Hosler, and W. R. Thurber, Magnetoresistance of Semiconducting $SrTiO_3$, Phys. Rev. **143**, 648 (1966).

[36] O. N. Tufte and E. L. Stelzer, Magnetoresistance in Semiconducting Strontium Titanate, Phys. Rev. **173**, 775 (1968).

[37] F. Kuchar and P. Frankus, Magnetoresistance of Cubic and Monodomain Tetragonal N-type Strontium Titanate, Phys. Rev. B **16**, 874 (1977).

[38] O. N. Tufte and E. L. Stelzer, Piezoresistive Properties of Reduced Strontium Titanate, Phys. Rev. **141**, 675 (1966).

[39] M. Cardona, Optical Properties and Band Structure of $SrTiO_3$ and $BaTiO_3$, Phys. Rev. **140**, A651 (1965).

[40] M. I. Cohen and R. F. Blunt, Optical Properties of $SrTiO_3$ in the Region of the Absorption Edge, Phys. Rev. **168**, 929 (1968).

[41] M. Capizzi and A. Frova, Optical Gap of Strontium Titanate (Deviation from Urbach Tail Behavior), Phys. Rev. Lett. **25**, 1298 (1970).

[42] Z. Sroubek, Electron Tunneling and Band Structure of $SrTiO_3$ and $KTaO_3$, Phys, Rev. B **2**, 3170 (1970).

[43] H. Uwe, T. Sakudo, and H. Yamaguchi, Interband Electronic Raman Scattering in $SrTiO_3$, Jpn. J. Appl. Phys. **Suppl.24-2**, 519 (1985).

[44] F. W. Lytle, X-Ray Diffractometry of Low-Temperature Phase Transformations in Strontium Titanate, J. Appl. Phys. **35**, 2212 (1964).

[45] K. A. Müller, W. Berlinger, M. Capizzi, and H. Gränicher, Monodomain Strontium Titanate, Solid State Commun. **8**, 549 (1970).

[46] W. Cochran, Crystal Stability and the Theory of Ferroelectricity, Adv. Phys. **9**, 387 (1960).

[47] P. A. Fleury, J. F. Scott, and J. M. Worlock, Soft Phonon Modes and the 110°K Phase Transition in $SrTiO_3$, Phys. Rev. Lett. **21**, 16 (1968).

[48] G. Shirane and Y. Yamada, Lattice-Dynamical Study of the 110°K Phase Transition in $SrTiO_3$, Phys. Rev. **177**, 858 (1969).

[49] K. W. Blazey, Optical Absorption Edge of $SrTiO_3$ Around the 105-K Phase Transition, Phys. Rev. Lett. **27**, 146 (1971).

[50] B. Berre, K. Fossheim, K. A. Müller, Critical Attenuation of Sound by Soft Modes in $SrTiO_3$, Phys .Rev. Lett. **23**, 589 (1969).

[51] Y. Yamada and G. Shirane, Neutron Scattering and Nature of the Soft Optical Phonon in $SrTiO_3$, J. Phys. Soc. Jpn. **26**, 396 (1969).

[52] J. Bardeen, L. N. Cooper, and J. R. Schrieffer, Theory of Superconductivity, Phys. Rev. **108**, 1957 (1957).

[53] M. L. Cohen, Superconductivity in Many-Valley Semiconductors and in Semimetals, Phys. Rev. **134**, A511 (1964).

[54] R. A. Hein, J. W. Gibson, R. Mazelsky, R. C. Miller, and J. K. Hulm, Superconductivity in Germanium Telluride, Phys. Rev. Lett. **12**, 320 (1964).

[55] E. Bustarret, C. Marcenat, P. Achatz, J. Kačmačik, F. Lévy, A. Huxley, L. Ortéga, E. Bourgeois, X. Blase, D. Débarre, and J. Boulmer, Superconductivity in Doped Cubic Silicon, Nature (London) **444**, 465 (2006).

[56] J. Appel, Soft-Mode Superconductivity in $SrTiO_{3-x}$, Phys. Rev. **180**, 508 (1969).

[57] K. L. Ngai, Two-Phonon Deformation Potential and Superconductivity in Degenerate Semiconductors, Phys. Rev. Lett. **32**, 215 (1974).

[58] Y. Takada, Theory of Superconductivity in Polar Semiconductors and Its Application to N-Type Semiconducting $SrTiO_3$, J. Phys. Soc. Jpn. **49**, 1267 (1980).

[59] R. H. Bube, *Photoelectronic Properties of Semiconductors* (Cambridge University Press, Cambridge, 1992).

[60] H. Yasunaga, Photo-Hall Effect in Strontium Titanate, J. Phys. Soc. Jpn. **24**, 1035 (1968).

[61] M. Takesada, T. Yagi, M. Itoh, and S. Koshihara, A Gigantic Photoinduced Dielectric Constant of Quantum Paraelectric Perovskite Oxides Observed under a Weak DC Electric Field, J . Phys. Soc. Jpn. **72**, 37 (2003).

[62] T. Ishikawa, M. Kurita, H. Shimoda, Y. Sakano, S. Koshihara, M. Itoh, and M. Takesada, Isotope Effect on Photoconductivity in Quantum Paraelectric $SrTiO_3$, J. Phys. Soc. Jpn. **73**, 1635 (2004).

[63] D. B. Chrisey and G. K. Hubler, *Pulsed Laser Deposition of Thin Films* (John Wiley & Sons, Inc., New York, 1994).

[64] W. Braun, *Applied RHEED: Reflection High-Energy Electron Diffraction During Crystal Growth* (Springer, Verlag, 1999).

[65] H. Katsu, H. Tanaka, and T. Kawai, Anomalous Photoconductivity in $SrTiO_3$, Jpn. J. Appl. Phys. **39**, 2657 (2000).

[66] Y. T. Sihvonen, Photoluminescence, Photocurrent, and Phase-Transition Correlation in $SrTiO_3$, J. Appl. Phys. **38**, 4431 (1967).

[67] A. L. Kholkin, V. A. Trepakov, G. A. Smolensky, Ju. V. Likholetov, V. D. Belyaev, and J. Auleutner, Transient Photocurrents and Photoconductivity in Strontium Titanate, Ferroelectrics **43**, 195 (1982).

[68] T. Sakudo, K. Hasebe, T. Ishizuka, H. Unoki, and K. Oka, Impurity Effect on the Structural Phase Transition in $SrTiO_3$, Jpn. J. Appl. Phys. **Suppl.20-4**, 47 (1981).

[69] S. H. Wemple, Some Transport Properties of Oxygen-Deficient Single-Crystal Potassium Tantalate ($KTaO_3$), Phys. Rev. **137**, A1575 (1965).

[70] K. Ohi and S. Takahashi, Photoconduction of Potassium Tantalate, J. Phys. Soc. Jpn. **31**, 614 (1971).

[71] K. A. Müller, W. Berlinger, and E. Tosatti, Indication for a Novel Phase in the Quantum Paraelectric Regime of $SrTiO_3$, Z. Phys. B **84**, 277 (1991).

[72] J. F. Scott and H. Ledbetter, Interpretation of Elastic Anomalies in $SrTiO_3$ at 37K, Z. Phys. B **104**, 635 (1997).

[73] L. Arzel, B. Hehlen, F. Dénoyer, R. Currat, K.-D. Liss, and E. Courtens, Observation of a Sample-Dependent 37 K Anomaly on the Lattice Parameters of Strontium Titanate, Europhys. Lett. **61**, 653 (2003).

[74] S. Katsumoto, F. Komori, N. Sano, and S. Kobayashi, Fine Tuning of Metal-Insulator Transition in $Al_{0.3}Ga_{0.7}As$ Using Persistent Photoconductivity, J. Phys. Soc. Jpn. **56**, 2259 (1987).

[75] P. W. Anderson, Absence of Diffusion in Certain Random Lattices, Phys. Rev. **109**, 1492 (1958).

[76] E. Abrahams, P. W. Anderson, D. C. Licciardello, and T. V. Ramakrishnan, Scaling Theory of Localization: Absence of Quantum Diffusion in Two Dimensions, Phys. Rev. Lett. **42**, 673 (1979).

[77] R. B. Laughlin, Quantized Hall Conductivity in Two Dimensions, Phys. Rev. B **23**, 5632 (1981).

[78] S. Hikami, A, I. Larkin, and Y. Nagaoka, Spin-Orbit Interaction and Magnetoresistance in the Two Dimensional Random System, Prog. Theor. Phys. **63**, 707 (1980).

[79] A. Kawabata, Theory of Negative Magnetoresistance in Three-Demensional Systems, Solid State Commun. **34**, 431 (1980).

[80] Z. Ovadyahu, Y. Gefen, and Y. Imry, Dimensionality Crossover Induced by a Magnetic Field in Thin Metallic Films, Phys. Rev. B **32**, 781 (1985).

[81] B. L. Al'tshuler and A. G. Aronov, Magnetoresistance of Thin Films and of Wires in a Longitudinal Magnetic Field, Pis'ma Zh. Eksp. Teor. Fiz. **33**, 515 (1981) [JETP Lett. **33**, 499 (1981)].

[82] R. C. Dynes and P. A. Lee, Localization, Interaction, and the Metal-Insulator Transition, Science **223**, 355 (1984).

[83] B. L. Al'tshuler, A. G. Aronov, A. I. Larkin, and D. E. Khmel'nitskiĭ, Anomalous Magnetoresistance in Semiconductors, Zh. Eksp. Teor. Fiz. **81**, 768 (1981) [Sov. Phys. JETP **54**, 411 (1981)].

[84] C. L. Chien and C. R. Westgate, *The Hall Effect and Its Applications* (Plenum Press, New York, 1979).

[85] E. H. Hall, On the New Action of Magnetism on a Permanent Electric Currents, Phil. Mag. Ser. 5 **10**, 301 (1880).

[86] E. H. Hall, On a New Action of the Magnet on Electric Current, Am. J. Math. **2**, 287 (1879).

[87] J. Inoue and H. Ohno, Taking the Hall Effect for a Spin, Science **309**, 2004 (2005).

[88] R. Karplus and J. M. Luttinger, Hall Effect in Ferromagnetics, Phys. Rev. **95**, 1154 (1954).

[89] J. Smit, The Spontaneous Hall Effect in Ferromagnetics I, Physica (Amsterdam) **21**, 877 (1955).

[90] L. Berger, Side-Jump Mechanism for the Hall Effect of Ferromagnets, Phys. Rev. B **2**, 4559 (1970).

[91] P. Matl, N. P. Ong, Y. F. Yan, Y. Q. Li, D. Studebaker, T. Baum, and G. Doubinina, Hall Effect of the Colossal Magnetoresistance Manganite $La_{1-x}Ca_xMnO_3$, Phys. Rev. B **57**, 10248 (1998).

[92] Y. Taguchi and Y. Tokura, Magnetotransport Phenomena in a Metallic Ferromagnet on the Verge of Mott Transition: $Sm_2Mo_2O_7$, Phys. Rev. B **60**, 10280 (1999).

[93] W.-L. Lee, S. Watauchi, V. L. Miller, R. J. Cava, and N. P. Ong, Dissipationless Anomalous Hall Current in the Ferromagnetic Spinel $CuCr_2Se_{4-x}Br_x$, Science **303** 1647 (2004).

[94] J. Ye, Y. B. Kim, A. J. Millis, B. I. Shraiman, P. Majumdar, and Z. Tešanović, Berry Phase Theory of the Anomalous Hall Effect: Application to Colossal Magnetoresistance Manganites, Phys. Rev. Lett. **83**, 3737 (1999).

[95] Y. Taguchi, Y. Oohara, H. Yoshizawa, N. Nagaosa, and Y. Tokura, Spin Chirality, Berry Phase, and Anomalous Hall Effect in a Frustrated Ferromagnet, Science **291**, 2537 (2001).

[96] S. Murakami, N. Nagaosa, and S.-C. Zhang, Dissipationless Quantum Spin Current at Room Temperature, Science **301**, 1348 (2003).

[97] Z. Fang, N .Nagaosa, K. S. Takahashi, A. Asamitsu, R. Mathieu, T. Ogasawara, H. Yamada, M. Kawasaki, Y. Tokura, and K. Terakura, The Anomalous Hall Effect and Magnetic Monopoles in Momentum Space, Science **302**, 92 (2003).

[98] J. M. Ziman, *Principles of the Theory of Solids*, 2nd ed. (Cambridge University Press, Cambridge, 1972).

[99] H .P. R. Frederikse and G. A. Candela, Magnetic Susceptibility of Insulating and Semiconducting Strontium Titanate, Phys. Rev. **147** 583 (1966).

[100] D. K. Schroder, *Semiconductor Material and Device Characterization*, 2nd ed. (John Wiley & Sons, Inc., New York, 1998).

[101] K. A. Müller, Paramagnetische Resonanz von Fe^{3+} in $SrTiO_3$ Einkristallen, Helv. Phys. Acta **31**, 173 (1958).

[102] M. Onoda and N. Nagaosa, Topological Nature of Anomalous Hall Effect in Ferromagnets, J. Phys. Soc. Jpn. **71**, 19 (2002).

[103] M . Kawasaki, K. Takahashi, T. Maeda, R. Tsuchiya, M. Shinohara, O. Ishiyama, T. Yonezawa, M. Yoshimoto, and H. Koinuma, Atomic Control of the $SrTiO_3$ Crystal Surface, Science **266**, 1540 (1994).

[104] M. Lippmaa, N. Nakagawa, M. Kawasaki, S. Ohashi, and H. Koinuma, Growth Mode Mapping of $SrTiO_3$ Epitaxy, Appl. Phys. Lett. **76**, 2439 (2000).

[105] T. Ohnishi, M. Lippmaa, T. Yamamoto, S. Meguro, and H. Koinuma, Improved Stoichiometry and Misfit Control in Perovskite Thin Film Formation at a Critical Fluence by Pulsed Laser Deposition, Appl. Phys. Lett. **87**, 241919 (2005).

[106] J. H. Haeni, C. D. Theis, D. G. Schlom, W. Tian X. Q. Pan, H. Chang, I. Takeuchi, and X.-D. Xiang, Epitaxial Growth of the First Five Members of the $Sr_{n+1}Ti_nO_{3n+1}$ Ruddlesden-Popper Homologous Series, Appl. Phys. Lett. **78**, 3292 (2001).

[107] M. Lippmaa, N. Nakagawa, M. Kawasaki, S. Ohashi, Y. Inaguma, M. Itoh, and H. Koinuma, Step-Flow Growth of $SrTiO_3$ Thin Films with a Dielectric Constant Exceeding 10^4, Appl. Phys. Lett. **74**, 3543 (1999).

[108] K. S. Takahashi, M. Gabay, D. Jaccard, K. Shibuya, T. Ohnishi, M. Lippmaa, and J. M. Triscone, Local Switching of Two-Dimensional Superconductivity Using the Ferroelectric Field Effect, Nature (London) **441**, 195 (2006).

[109] K. Eisenbeiser, J. M. Finder, Z. Yu, J. Ramdani, J. A. Curless, J. A. Hallmark, R. Droopad, W. J. Ooms, L. Salem, S. Bradshaw, and C. D. Overgaard, Field Effect Transistors with $SrTiO_3$ Gate Dielectric on Si, Appl. Phys. Lett. **76**, 1324 (2000).

[110] K. Shimamura, H. Tabata, H. Takeda, V. V. Kochurikhin, and T. Fukuda, Growth and Characterization of (La,Sr)(Al,Ta)O_3 Single Crystals as Substrates for GaN Epitaxial Growth, J. Cryst. Growth **194**, 209 (1998).

[111] S. C. Tidrow, A. Tauber, W. D. Wilber, R. T. Lareau, C. D. Brandle, G. W. Berkstresser, A. J. Ven Graitis, D. M. Potrepka, J. I. Budnick, and J. Z. Wu, New Substrates for HTSC Microwave Devices, IEEE Trans. Appl. Supercond. **7**, 1766 (1997).

[112] H.-C. Li, W. Si, A. D. West, and X. X. Xi, Near Single Crystal-Level Dielectric Loss and Nonlinearity in Pulsed Laser Deposited $SrTiO_3$ Thin Films, Appl. Phys. Lett. **73**, 190 (1998).

[113] A. Leitner, C. T. Rogers, J. C. Price, D. A. Rudman, and D. R. Herman, Pulsed Laser Deposition of Superconducting Nb-Doped Strontium Titanate, Appl. Phys. Lett. **72**, 3065 (1998).

[114] A. A. Sirenko, C. Bernhard, A. Golnik, A. M. Clark, J. Hao, W. Si, and X. X. Xi, Soft-Mode Hardening in $SrTiO_3$ thin films, Nature (London) **404**, 373 (2000).

[115] W. Ramadan, S. B. Ogale, S. Dhar, S. X. Zhang, D. C. Kundaliya, I. Satoh, and T. Venkatesan, Substrate-Induced Strain Effects on the Transport Properties of Pulsed Laser-Deposited Nb-Doped $SrTiO_3$ Films, Appl. Phys. Lett. **88**, 142903 (2006).

[116] Y. L. Qin, C. L. Jia, K. Urban, J. H. Hao, and X. X. Xi, Dislocations in $SrTiO_3$ Thin Films Grown on $LaAlO_3$ Substrates, J. Mater. Res. **17**, 3117 (2002).

[117] K. Terai, M. Lippmaa, P. Ahmet, T. Chikyow, T. Fuji, H. Koinuma, and M. Kawasaki, In-Plane Lattice Constant Tuning of an Oxide Substrate with $Ba_{1-x}Sr_xTiO_3$ and $BaTiO_3$ Buffer Layers, Appl. Phys. Lett. **80**, 4437 (2002).

[118] Y. Tokura, Photoinduced Phase Transition: A Tool for Generating a Hidden State of Matter, J. Phys. Soc. Jpn. **75**, 011001 (2006).

[119] S. Nozawa, T. Iwazumi, and H. Osawa, Direct Observation of the Quantum Fluctuation Controlled by Ultraviolet Irradiation in $SrTiO_3$, Phys. Rev. B **72**, 121101 (2005).

Acknowledgments

Overall this work was carried out with considerate support by the members of Hwang laboratory. Throughout this work, Prof. Harold Y. Hwang gave us leading advice when we were stuck, gave us informative suggestions, and guided us from the beginning stage to the end. We naively feel invaluable impression on his belief both as a researcher and as a educator. We are heartily thankful his encouraging and motivating words for us.

We appreciate Prof. Hidenori Takagi and his members for letting us use one of their furnace. They also gave us an opportunity to introduce and discuss our results our work. The discussion was quite useful and help us to interpret our experimental results. The content in Chapter 5 in this thesis is greatly indebted to the discussion.

We also appreciate Prof. Mikk Lippmaa and his members for allowing us to use their stylus profilometer. In particular, Prof. Lippmaa, Dr. Ohnishi, and Dr. Shibuya gave us significant advice for thin film fabrication. The content in Chapter 7 is strongly affected by their useful suggestions as well as their impressive work.

We are grateful to Prof. Masashi Kawasaki and his members for giving us an opportunity to give a brief presentation on our work. In particular, Prof. Kawasaki, Dr. Ohtomo, Dr. Tsukazaki and Dr. Ueno had intensive discussions with us and their wide knowledge strongly helped our work. Their enthusiasm about science frequently encouraged us as well. We would like thank Prof. Naoto Nagaosa and Dr. Masaru Onoda for allowing us to present our work and they had discussion with us. In particular, a theoretical aspect of this thesis is heavily indebted to their suggestions.

The research associate, Dr. Tomofumi Susaki, always supported us to a great extent. We often consulted him and he gave us useful advice. We are profoundly thankful for his intensive instruction.

We are really thankful to our members: Dr. Kei S. Takahashi, Dr. Shunsuke Tsuda, Dr. Jong Hyun Song, Mr. Yasuyuki Hikita, Mr. Yasushige Mukunoki, Mr. Shin Yoshida, Mr. Motoshi Nakayama, Mr. Takuya Higuchi, and Mr. Takeaki Yazima. We are also thankful to our former members: Dr. Naoyuki Nakagawa, Dr. Yasushi Hotta, Mr. Shinsuke Nishiki, and Mr. Kohki Fukui. Throughout this work, they always taught us various kinds of suggestions and motivated us.

We would like to express our cordial appreciation for our secretary, Mrs. Makiko Tanaka. She always supported us and gave us ease for a time. She also generously accepted tiresome office work for us without any complaints. Our work has been indirectly but greatly supported by her.

2007　Master's thesis: Transport Properties of Photocarrier-Doped $SrTiO_3$

(光キャリアドープされたチタン酸ストロンチウムの輸送特性)

56117　Yusuke Kozuka